GEOMORPHIC EVALUATION OF THE GOOSE LAKE FAULT AND FLUVIAL TERRACES AT THE YAGER CREEK–VAN DUZEN RIVER CONFLUENCE, NORTHERN COASTAL CALIFORNIA

By

Samuel Edward Bold

A Thesis Presented to

The Faculty of California Polytechnic State University, Humboldt

In Partial Fulfillment of the Requirements for the Degree

Master of Science in Environmental Systems: Geology

Committee Membership

Dr. Melanie Michalak, Committee Chair

Dr. Harvey Kelsey, Committee Member

Mr. Tyler Ladinsky, Committee Member

Dr. Robert Witter, Committee Member

Dr. Margaret Lang, Graduate Program Coordinator

May 2022

ABSTRACT

GEOMORPHIC EVALUATION OF THE GOOSE LAKE FAULT AND FLUVIAL TERRACES AT THE YAGER CREEK–VAN DUZEN RIVER CONFLUENCE, NORTHERN COASTAL CALIFORNIA

Samuel Edward Bold

Upper-plate deformation in the southern Cascadia subduction zone is dynamic and complex, situated in the transition between northward translation to westward convergence. Rock uplift and incision rates characteristic of this dynamic region are preserved in suites of fluvial and marine terraces. Fluvial terraces at the Yager Creek–Van Duzen River confluence record fluvial incision rates, and are crosscut by the understudied Goose Lake fault, an upper plate structure. In this work, I use high resolution lidar imagery to map terrace surfaces, and use optically stimulated luminescence, radiocarbon, and Beryllium-10 geochronology to bracket terrace ages and calculate incision and slip rates. With GIS analysis, I mapped 21 fluvial terrace suites and calculated slope aspect for each surface. I mapped three strands of the Goose Lake fault, and calculated vertical separation across each strand. Results show terrace surfaces tilt northward up to 8.6°, and the Goose Lake fault progressively vertically separates terrace surfaces up to 16.6 m up to the south. Age determinations for ten samples from five terraces reveal depositional ages for terrace cover sediment ranging from at least ~47 to ~9 ka. Channel incision rates range from 2.3 to 5.2 mm/yr, and vertical slip rates on the Goose Lake fault range from 0.03 to 0.87 mm/yr. Incision rates, interpreted as rock uplift,

indicate regionally rapid uplift in the lower Van Duzen River valley. In contrast, relatively slow slip rates of the Goose Lake fault indicate a distinct and less significant mechanism.

ACKNOWLEDGEMENTS

I am grateful to many individuals and organizations who have helped make this project possible through personal and financial support. Melanie: you give so much of yourself to your students; thank you for your mentorship, you have been an advocate for my education, and I have learned so much getting to work alongside you. Harvey, Rob, and Tyler: thank you for your thoughtful engagement and guidance from the start of trenching, through the completion of this work; the way I was so wholly incorporated has been invaluable. Mark and Jay: thank you for your expertise, assisting me in the field, and on the computer; you made yourselves available, and I appreciate you for it. The Humboldt geology faculty and staff: courses and research opportunities in this program have such depth because of your genuine care for the growth of us students; your dedication is clear, and it is appreciated. Finally, to my family and friends, for supporting me in such a steady way through this project. Nobody has had a smooth ride over these last two years, so thank you for being so generous to let me lean on you while I've worked on this.

Funding included the Humboldt geology department for the Bud Burke and Geology Opportunities field scholarships, the Geological Society of America Graduate Student Research Grants, and the National Earthquake Hazard Reduction Program.

TABLE OF CONTENTS

LIST OF TABLES

LIST OF FIGURES

LIST OF APPENDICES

INTRODUCTION

Active river channels are useful landforms for studying uplift of landscapes because when active river channels and their floodplains are abandoned and preserved as terraces, they become a physical progressive record of landscape evolution (e.g., Merritts, 2007). Moreover, because terrace surfaces form at predictable and consistent slopes, they capture surface deformation such as faulting, folding or broad-scale tilting (e.g., Molnar et al., 1994; Lave and Avouac, 2000). If depositional ages can be constrained for terraces using methods such as radiocarbon (^{14}C) (e.g., Longin, 1971), optically stimulated luminescence (OSL) (e.g., Aitken, 1998), or Beryllium-10 (^{10}Be) (e.g., Gosse and Phillips, 2001), rates of deformation or uplift can be estimated. Remote imagery, particularly high-resolution imagery such as light detection and ranging (lidar), is ideal for investigating river terraces because the scale of research questions can span tens of kilometers and be difficult to observe and map in the field. Geographic information systems (GIS) software can accurately map these features and analyze broad swaths for possible surface deformation.

The southern Cascadia subduction zone (SCSZ) is a region in tectonic transition between the San Andreas transform boundary (SAF) to the Cascadia megathrust (McKenzie and Furlong, 2021) (Figure 1). Here, Quaternary thrusts and folds, including the Little Salmon fault zone (LSF) (Ogle, 1953; Clarke and Carver, 1992), are observed on- and offshore, deforming preexisting structures within the Humboldt Basin (McCrory, 1995).

In the eastern extent of the Humboldt basin, in the lower Van Duzen River valley, multiple flights of terraces are present adjacent to the confluence of Yager Creek and the Van Duzen River (Ogle, 1953; O'Dea, 1992) (Figure 2). Two fault systems that trend through the confluence area are the LSF, (Ogle, 1953; Woodward-Clyde Consultants, 1980; Carver and Burke, 1988; Witter et al., 2002; Hemphill-Haley and Witter, 2006; Ladinsky et al., 2020), and the Goose Lake fault (GLF) (Woodward-Clyde Consultants, 1980; Ladinsky et al., 2020). Two paleoseismic studies have targeted the GLF (Woodward-Clyde Consultants, 1980; Ladinsky et al., 2020), however, the acquisition of high resolution lidar (USGS, 2020) justifies renewed investigation of the area in a GIS based approach. Here, I focus on two major research objectives: i) detailed mapping and geochronologic investigation of terrace surfaces surrounding the Yager Creek–Van Duzen River confluence, and ii) quantifying terrace deformation across multiple strands of the Goose Lake fault. By combining mapping with geochronological age-dating, I address the following research questions: i) what is the rate and extent of terrace formation and deformation? And, ii) what tectonic mechanisms are driving surface incision and deformation?

SETTING

Tectonics

The Pacific, North American, and Gorda segment of the Juan de Fuca plates meet at the latitude of the Mendocino triple Junction (MTJ), ~40.5° N, 20 km offshore of northern California (Merritts, 1996; Kelsey and Carver, 1988; Wells, 1998; Furlong and Schwartz, 2004; Williams et al., 2006). The MTJ is a migratory feature, moving northward over the past ~30 Ma (Atwater, 1970). In the Mendocino crustal conveyor model of Furlong and Govers (1999), the migration of the MTJ affects crustal structure; the crust thickens, subsequently thins, and rapidly uplifts in the wake of MTJ migration northward. Geochemical signatures of volcanism, geomorphic river drainage reorganization, and locally high uplift rates are associated with the ephemeral passing of the MTJ (Furlong et al., 1989; Lock et al., 2006; Merritts and Bull, 1989).

Geodetic measurements surrounding the MTJ show an average of 52 mm/yr northwest dextral slip along Pacific-North American boundary, and 31 mm/yr of northeast convergence along the Gorda–North American plates over the past 2–3 Ma (McKenzie and Furlong, 2021). Marine terraces show uplift rates of up to 4.0 mm/yr closest to the MTJ, with lesser rates of 0.4–1.2 mm/yr further south (Merritts and Bull, 1989). In the upper plate, from ~40°–41° N, numerous offshore and onshore faults with active, complex deformation accommodate plate convergence (Merritts and Vincent,

1989; Clarke and Carver, 1992; Dengler et al., 1995; McCrory, 2000; Oppenheimer et al., 1993).

Upper Plate Deformation

Crustal deformation of the North American plate between the San Andreas transform fault and the Cascadia subduction zone (Figure 1) results from frequent seismicity in a structurally complex region (e.g., McPherson, 1992; Rollins and Stein, 2009). In the SCSZ, Quaternary folds and thrust faults come onshore, deforming preexisting crustal structures (Carver et al., 1986; Kelsey, 2001; Clarke and Carver, 1992). Strain partitioning likely plays a major role in the distribution and style of faulting (McCrory, 2000; Ladinsky, 2020). From north to south, major upper plate structures within the region relevant to this thesis include i) the Little Salmon fault (LSF), ii) the Goose Lake fault (GLF), and iii) the Russ fault (Figure 1C). Lesser studied structures include the Van Duzen fault (Nicovich, 2015), and the Grizzly Bluff anticline (Gordon, 2009).

The LSF is the southernmost major thrust fault in the SCSZ (Kelsey and Carver, 1988; McCrory, 2000). The LSF dips north (10°–30°), with an average slip rate ranging from 6–12 mm/yr, and strikes from N60W at its southeastern in the Van Duzen River basin at ~40°N, to N20W at its western offshore end at ~40.5°N (Ogle, 1953; Woodward-Clyde Consultants, 1980; Carver and Burke, 1992; Vadurro et al., 2006; Ladinsky et al., 2020). Three distinct segments along the LSF have been recognized by some workers (western, central, eastern) (Carver and Burke, 1988; Clarke and Carver, 1992; Witter et

al., 2002; Hemphill-Haley and Witter, 2006; Ladinsky et al, 2020). The possibility of coseismic rupture of the LSF with the Cascadia megathrust is a principal question, particularly in the western and central segments, but the details of this scenario remain unresolved (Clarke and Carver, 1992; Ladinsky et al., 2020).

The central segment of the LSF bounds the northern part of the study area. Studies indicate the fault slipped during three Holocene earthquakes (Ladinsky et al., 2020), with additional pre-Holocene earthquakes documented by Hemphill-Haley and Witter (2006). Evidence shows three to four earthquakes in the western segment in the last two thousand years, possibly coincident with or overlapping with Cascadia megathrust rupture (Carver and Burke, 1988; Clarke and Carver, 1992; Witter et al., 2002).

The GLF strikes east-west and is located approximately 4 km northeast of the Van Duzen River–Eel River confluence, about two km south of the central segment of the LSF (Figure 1). Three strands of the GLF are mapped (Woodward-Clyde Consultants, 1980; O'Dea, 1992; Ladinsky, et al., 2020). The central strand has been investigated via trenching on two occasions which show the GLF directly below the surface is a south-side-up, high angle reverse fault (Woodward-Clyde Consultants, 1980; Ladinsky, et al., 2020). Based on the similar strike and close proximity to the LSF, workers have hypothesized the GLF may be part of the LSF system. However, recent seismic reflection data and industry well logs leave open the possibility that the GLF dips to the south, making such a relation unlikely (Verhey, 2006; Gordon, 2009).

The next major, potentially active, fault to the south of the GLF in the SCSZ is the Russ fault, striking ~N80W (McCrory, 2000). The Russ fault is located at ~40.5° N and mapped as a high angle (85°) fault dipping to the south, with kinematics that are not well understood (Ogle, 1953; Carver et al., 1986; McCrory, 2000, McLaughlin et al., 2000). North of the Russ fault along the coast, structures are mapped with dominant dip-slip motion (Carver, Burke, and Kelsey, 1986; Clarke and Carver, 1992) reflecting strain associated with the fold-thrust belt of the SCSZ.

Terrace Formation

Terraces are ubiquitous throughout the MTJ along coastal and inland watersheds, and reveal landscape changes driven by tectonic and climatic forces (Merritts, 2007). Flights of marine terraces (Merritts and Bull, 1989; Merritts and Vincent, 1989; Crawford, 2015; Hartshorn, 2017), and fluvial terraces (O'Dea, 1992; Stallman, 2003; Nicovich, 2015; Robinson, 2016), when paired with sea level curves or chronologic data, can provide parameters to calculate uplift rates, upper plate fault activity, and climatic changes.

Merritts and Bull (1989) use marine terraces to identify variable coastal uplift rates along sites ~40.4°–40.5° N, latitudes nearby the MTJ. Over time, rates vary from 0.5 to 4.0 mm/yr, and compare uplift rates with proximity to the MTJ. Similarly, Merritts and Vincent (1989) address channel gradient response with respect to uplift rates near the MTJ. Crawford (2015) finds evidence for Holocene coseismic uplift in the last 6000 ka by mapping marine terraces near Cape Mendocino. Building on this work, Hartshorn

(2017) also used lidar to map marine terraces near Cape Mendocino, finding increased uplift rates of 2.7–3.8 mm/yr in Holocene terraces compared to Pleistocene terraces of less than 0.4 mm/yr.

Within the study area for this thesis, O'Dea (1992) investigated the fluvial terraces near the Yager Creek–Van Duzen River confluence, assigning ages to terraces based on soil development. O'Dea (1992) correlated times of terrace strath formation to sea level high stands. Further north, Stallman (2003) mapped and dated, with radiocarbon (C14), strath terraces in the valley of the North Fork Elk River. Stallman (2003) reported relatively higher (0.8–1.4 mm/yr) incision rates in the last 20 ka, with longer term (up to 40 ka) uplift rates being more subdued (~0.5 mm/yr). Stallman (2003) interprets strath terrace formation to be associated with climatic forcing. Ten km upstream of the study area along the Van Duzen River, Nicovich (2015) mapped fluvial terraces and trenched a scarp across the Van Duzen fault, estimating a rate of 0.05–0.5 mm/yr of slip over the last 262 ka, assuming dip-slip motion, and using implied incision rates from published uplift rates. Nicovich (2015) associates the Van Duzen fault with the Little Salmon fault zone. Robinson (2016) mapped fluvial terraces and provided optically stimulated luminescence (OSL) terrace surface ages, relating climate forcing and MTJ migration to changes in river gradients within the Mattole watershed over the past 17 ka.

In the above-described broad body of regional work, the investigations consistently show rapid, localized responses of the landscape to tectonic and climatic forces. Varied conclusions may reflect variable spatiotemporal tectonic conditions throughout the MTJ.

Study Area

The study area is in the vicinity of Hydesville, in northern California (Fig 1C). Town centers are mostly consolidated to the flat basin areas of ~20–200 meter elevation, occupied by residents with grazeland properties. Dense redwood and mixed conifer forests blanket surrounding mountains up to ~600 meters elevation. The northern California coastal climate is temperate yet cool, with about 120 cm of rainfall each year (NOAA, 2021).

The study site is bounded by the Eel River to the west, the LSF to the north, Yager Creek the valley to the east, and the Van Duzen River to the south (Figure 2). Near the study area's southeast corner, Yager Creek flows S20°W into the Van Duzen River, which in-turn flows N70°W and merges with the Eel River. Other smaller tributaries within the terraced area of interest include the Wolverton Gulch, Cuddleback Creek, and Wilson Creek, all which flow south into the Van Duzen (Figure 2). Within the study area, the Van Duzen River flows within a ~60 m wide active channel bordered by a floodplain that is up to ~400 m wide. The smaller, narrower active channel of Yager Creek is ~25 m wide with a maximum floodplain width of ~100 meters. The Van Duzen River meanders broadly and rapidly based on its wide banks of unvegetated gravel bars. Conversely, Yager Creek has heavily vegetated banks, indicating a relatively narrow, stable channel.

Yager Creek and the Van Duzen River terraces are nonpaired along either side of the respective channels. The best preserved and most extensive terraces are northwest of the Yager–Van Duzen confluence, with significantly less terraces northeast of the

confluence, and very limited preservation south of the Van Duzen River (Ogle, 1953; O'Dea, 1992). Based on terrace preservation, this study directed investigations to terraces northwest of the confluence. Fluvial terraces surrounding the Yager Creek–Van Duzen River confluence are preserved and crosscut by three east-west trending traces of the Goose Lake fault (Ogle, 1953; O'Dea, 1992; McLaughlin et al., 2000; Ladinsky, et al., 2020).

Lithology

Lithologic units in the study area, which collectively range in texture from clay to silt to sand to gravel and boulder, include Pleistocene-Holocene terrace and alluvial sediments overlying Pliocene and Pleistocene nonmarine sediments (Ogle, 1953; McLaughlin et al., 2000) (Figure 1C). Ogle (1953) distinguishes relative age of alluvium and terrace deposits based on elevation. Ogle's (1953) mapped units are Alluvium, Old alluvium, Young stream terrace deposits, Undifferentiated terrace deposits, Rohnerville fm., and Hookton fm. Older underlying units include the Carlotta formation and Scotia Bluffs sandstone, both of which are upper units of the Wildcat group. The Carlotta formation and Scotia Bluffs sandstone are mapped only in the margins of the study area.

APPROACH

To better understand the behavior of the GLF and investigate the effect of regional tectonics, I executed an investigation of fluvial terraces using image-based mapping and geochronology. I used newly available lidar (USGS, 2020) to construct digital elevation models (DEM) (Figure 2) and analyzed data in ArcMap and Microsoft Excel. By combining mapping with geochronology (^{10}Be, OSL, C14 age-determination techniques), the goals were to (a) improve existing fault and terrace maps, (b) determine local incision rates, (c) characterize the GLF in detail, and (d) propose a more substantiated and better constrained faulting model that aligns with our understanding of regional tectonic geomorphology.

The next section outlines methodology in three parts: terrace mapping and analysis, structure mapping and analysis, and geochronology analysis.

Terrace Mapping and Analysis

The following six steps build upon one another to comprehensively map terraces and extract elevation data relevant for investigating rates of landscape change.

Terrace Surface Identification

Lidar data published by the USGS were downloaded from The National Map formatted as '.las' files (2020). These were converted from '.las' files to raster datasets using ArcMap, and express elevation values of bare earth surface. This raster layer then

served as the base DEM (Figure 2), which was used as input for constructing various layers using the ArcMap toolbox.

Guided by general principles of fluvial terrace formation (Merritts, 2007), and by previously mapped terrace deposits in the study area (Ogle, 1953; Woodward-Clyde Consultants, 1980; O'Dea, 1992; McLaughlin et al., 2000; Ladinsky, et al., 2020), all low-sloped flat surfaces were assumed to be fluvially deposited terraces. Surfaces were identified at ~1:1500 scale, using 1.5° and 3.0° slope shade rasters (Figure 3), two-meter contour, and hill shade layers. Polygons were drawn to encompass individual surfaces and only included areas with a maximum of 3.0° slope. Features identified as roads, slumping, and sloping edges were all excluded from polygons, for sake of terrace dataset precision. Polygons were delineated where elevation changes were consistent, and these changes were at least ~1.5 meters.

Terrace Assignments to Source Channel

Each terrace had to be assigned a depositional channel, either Yager Creek or the Van Duzen River, because to calculate incision rates, I had to determine an elevation datum for each terrace. Criteria for depositional channel assignment was based on typical terrace models (Cowgill, 2007, Merritts, 2007; McCalpin, 2009) and I specifically used proximity, topography, geometry, and terrace riser orientation as distinguishing factors. Proximity and topography were relied on for the majority of terraces, with the exception of confluence areas. Here, terrace long axis and long edge were compared to channel flow orientation, assuming that the depositional channel would be most parallel to such. If this was still indistinguishable, back edge orientation was prioritized next, inferring

that although a single terrace may have been overprinted by multiple channels, back edge orientation revealed the most recent formation source.

Depositional channel assignments were recorded as an attribute field within the terrace polygon feature layer, but also converted to a raster layer, using the ‘feature to raster’ tool. This layer was later reincorporated as an attribute to other features which coincide with terraces.

Relative Chronology Assignment

Each terrace polygon was assigned a relative depositional age (Figure 4). I used a single numbering scheme (i.e., 1, 2, 3, n…) for all terraces in the study area. The lowest surfaces adjacent to the active channel were assigned ‘Qt0’, and subsequently higher terraces, observed to be separated by at least 1.5 m elevation, were assigned a sequential number (Qt1, Qt2...Qt20). Terraces and terrace sequences were not all equally preserved, so some adjacent terraces were not assigned to the sequentially next-highest number.

Terrace number assignments were recorded as an attribute field within the terrace polygon feature layer, but also converted to a raster layer, using the ‘feature to raster’ tool. This layer was later reincorporated as an attribute to other features which coincide with terraces.

Slope Aspect

A surface elevation profile was produced as a first–order slope–aspect analysis. The profile includes elevations across a broad swath projected onto a single plane. Elevation points were extracted from the DEM every five meters along a lineation in ArcMap, then plotted in Microsoft Excel (Figure 5).

Each terrace polygon was analyzed in ArcMap for average slope and aspect to investigate trends and interpret possible deformation (Figure 6). Terraces are assumed to have been originally deposited with a slope and aspect similar to their associated channels. Significant deviation from original slope and aspect may reveal tectonic influences (McCalpin, 2009).

Slope and aspect analyses each were distinct processes, but required the same two initial raster layers in ArcMap. First, a new DEM was trimmed ('trimmed DEM') to terrace polygon extents using the 'extract by mask' tool with the full DEM as a raster input and the terrace polygon layer as the mask. Second, a raster layer with zoned cell values ('zonal polygon raster') matching terrace polygons was created using the 'polygon to raster' tool.

For slope analysis, the 'slope' tool was used on the trimmed DEM, producing a degree value per cell. The 'zonal statistics' tool was used next, using the previous output layer as input, and the zonal polygon raster to calculate an average slope per terrace.

For aspect analysis, a dominant aspect was ultimately assigned per polygon, binned into 30° ranges, in twelve azimuthal surface dip directions. First, the 'aspect' tool was used, with the trimmed DEM as input, outputting an azimuth direction per cell. Next, the 'reclassify' tool binned each cell into their respective categories, using integers to represent the 12 directions.

Reclassification was used to simplify output results, but also to combine north values 345–360 and 000–015 together. The 'zonal statistics' tool was used with the reclassified values and the zonal polygon raster to calculate the majority value for each

polygon. The majority value, rather than the average value, was used to represent the overall direction of a surface.

Slope and aspect raster layers were each reincorporated into the terrace polygon feature layer as an attribute using the ‘join field’ tool. Polygon shapefile was the ‘input field’, the ‘objectid’ was the shared attribute used for ‘input join field’, and the ‘output join field’ was the slope or aspect value which is desired to join.

Hydrology Analysis

Stream channel paths were extracted from lidar data using the ‘hydrology’ toolbox in ArcMap. The following series of steps identified and traced points of lowest elevation through the DEM to map a stream channel thalweg and produce representative line features. Thalweg heights were later used to compare to terrace heights. Unless otherwise noted, each step in this series used the previous output layer as the input.

The ‘fill’ tool was used first with the DEM to interpolate any missing, blank cells in it, which is based on nearby values. The ‘flow direction’ tool was next, and assigned a steepest direction to each cell based on elevations. Then, ‘flow accumulation’ tool calculated how many cells are uphill of, and theoretically should flow into, each one. The ‘reclassify’ tool next identified and extracted cells with raster values above a certain threshold. The underlying assumption here is that the thalweg has the highest accumulation, so the intent is to identify such. Different threshold values were appropriate for different watershed sizes, and 1,000,000 was the threshold used here. The actual value of the cells is not important, only the lineation that is created by qualifying cells, so all points above the threshold are reclassified as ‘1’ and all values below are

reclassified as ‘NoData’ (scrapped). The Symbology tab within layer Properties, and Google Maps imagery, helped to estimate a target threshold value, and gauge output accuracy, respectively. The output layer generates lineations for more than just a single target channel, but was easily trimmed manually. Finally, the ‘stream to feature’ tool created line features from all desired line segments.

Point Cloud Analysis

A point grid of elevation values was extracted from ArcMap and graphed in Microsoft Excel as a scatter plot to observe terrace surfaces relative to active channel streambed (Yager Creek, and Van Duzen River, respectively). Plots were used to observe possible deviations which may reveal structural significance (e.g., Bender et al., 2016), and to calculate terrace heights above their depositional stream channel, later used to calculate incision rates.

To create the point grid, the ‘fishnet’ tool was executed by inputting the terrace-trimmed DEM raster (described in “Slope Aspect” section). A resolution of 25 square meters was selected, based on trial-and-error, to reveal a representative dataset (“fishnet grid”). Next, ‘extract multi values to points’ tool was applied to the fishnet grid to assign terrace generation number, channel association, and elevation, to each point.

The second step was to run the ‘locate features along routes’ tool which disperses points along downstream distance of a line feature (here: Yager Creek and the Van Duzen River). As a precursor, a route is created using ‘create routes (linear referencing)’ tool. A straight line for each channel is used for the route. The Yager Creek line is drawn from the opening of the river valley to the confluence with the Van Duzen River, and the Van

Duzen River line is drawn from the confluence with Yager Creek to the confluence with the Eel River. If a curved or jointed line is used as a route, points cluster around nearby bends, rather than distribute evenly. Results are extracted into '.txt' file format and imported into Microsoft Excel.

The 'locate features along routes' tool was also executed for streambed elevation values. Thalweg line features were converted to points using the 'generate points along lines' tool (here: five-meter distance). Elevation values were then assigned to the resulting point set with the 'extract values to points' tool. Again, 'locate features along route' tool was executed for each Yager Creek and Van Duzen River route. The result was a set of streambed values along a distance that is equivalent to that which was used for the fishnet terrace point grid. This dataset was also executed as a '.txt' file and imported into Excel. Streambed and fishnet grid could be processed together, but keeping them separate helps with data organization, since the fishnet grid is large, with over 34,000 terrace points.

Two scatter plots ("point clouds") are constructed in Excel using exported fishnet grid and streambed point datasets, one relative to Yager Creek (Appendix A: Point cloud of surface elevation values across all terrace surfaces northwest of Yager Creek–Van Duzen River confluence, from Yager Creek perspective.) and one relative to the Van Duzen River (Appendix B). Axes are 'downstream distance' versus 'elevation,' for each channel. While the dataset is the same for each plot, the data are organized in two perspectives (each channel). Exported point sets included a 'measure' column, representing the downstream distance along the route parallel to the point feature, and a 'distance' column showing how far the feature

was from the route (i.e., the projected distance). The measure column was used for the horizontal axis, and the ‘distance’ value was disregarded. Each terrace generation, and the streambed, was added to the plot as a separate dataset in order to visually differentiate each surface, and in order to omit data from tributaries Wolverton Gulch, Wilson Creek, and Cuddleback Creek. Surface data, which show deformation in the study area, are presented relative to Yager Creek (Figure 7).

Finally, a best-fit lineation representing channel streambed was plotted, so elevation values could be subtracted from terrace heights (to be used for incision rate analysis). The regression formula was used to calculate individual streambed heights at each fishnet point x-value, then subtracted from that terrace point y-value, producing a ‘height above channel’ for each fishnet point. This method works with an underlying caveat that no significant knickpoints in the streambed profiles were observed and that regression lines represented points with a precision of R^2=0.99 for each channel.

Structure Mapping

To characterize surface rupture and develop fault models at depth, fault lineation mapping and vertical separation analysis were performed on the lidar DEM using ArcMap.

Fault Lineation Mapping

GLF mapping was guided by previous studies (Woodward-Clyde Consultants, 1980; O’Dea, 1992; Ladinsky, et al., 2020), but mapping presented in this thesis is based on direct observations from the lidar-derived DEM. However, where lineations were not

identifiable in the DEM, mapping of the LSF, Ferndale fault, and Alton anticline refer to published work (McLaughlin et al., 2000; Ladinsky, et al., 2020, USGS and CGS, 2020). Surface lineations in the mapping area were identified in a similar method as the terrace mapping campaign. ArcMap was used at ~1:1500 scale, with 1.5° and 3.0° slope shade rasters, two-meter contour, and hill shade raster layers draped over the DEM. It is assumed that lineations in the mapping area are anthropogenic, erosional, fluvial, or seismogenic.

Certain distinguishing factors served as evidence for interpreting lineation type. Human structures are inorganically straight, smooth, or hinged. Fluvial lineations (overprinting from ancestral meanders or floods) tend to bow in swarms, trend similar to flow direction, and are most prevalent in floodplain or young surfaces near active channels. Hillslope derived lineations, such as ravines or gullies, tend to project radially from a given peak, and terminate at the intersection of a basal stream channel or plain (Anderson and Anderson, 2011). Since faults are structures at depth, the lineations they create are not necessarily determined by topography, and therefore may uniquely crosscut the landscape. Lineation mapping was qualified into categories based on confidence level of location, and certainty of fault presence consulting previously published mapping (Figure 4).

Vertical Separation Analysis

Vertical separation analysis focused on the three mapped strands of the GLF within the study area. I identified vertical separation between equivalent terrace surfaces across each fault strand to compare apparent offset across the GLF. If the fault ruptured

multiple times penecontemporaneous with formation of the Yager Creek terrace sequence (Qt3 through Qt12), then the fault should express progressive separation with older terraces being progressively more separated (Kaneda et al., 2008b; McCalpin, 2009).

I assumed the most objective comparison of terrace elevation across a fault strand was to measure separation values at equal distances along each fault. This method showed relative separations between terraces but did not provide insight into dip direction or faulting style.

In ArcMap, the ‘buffer’ editor tool is used for the GLF line features within the study area to automatically generate corridors along either side of each strand. Swatch widths were 100, 150, and 150 meters for southern, central, and northern strands (respectively). The ‘generate points along line’ tool was used for these resulting buffer corridors (five-meter interval). Elevation and terrace values were added to point sets using the ‘extract multi values to points’ tool, using relative chronology raster and DEM as input layers. The ‘locate features along route’ tool was executed, using fault lineations as routes. The resulting data were exported as a ‘.txt’ file and imported into Microsoft Excel.

Only pairs of points mapped as the same terrace generation were included in this analysis. Many points were outside of mapped terrace polygons, or some pairs were assigned different terrace generations, but this meant there was high confidence in the points which were retained. Separation values were plotted, along-strike distance versus separation height, per strand (Figure 8). The extent of each terrace was respectively shaded and labeled.

Geochronology

Sampling

Terrace surfaces were sampled and analyzed for depositional age with a goal to calculate local incision rates. I used three geochronological methods, ^{14}C, OSL, and ^{10}Be. While field sampling opportunities were limited, I prioritized sample locations such as: public right-of-ways at road cut outcrops, shoulders, and on private property with permission granted. Sites were targeted wherever feasible and within mapped terrace extents.

Radiocarbon. ^{14}C was used for age determinations for charcoal found in cover sediments on terrace Qt7 (samples QYt2-03-031921R and QYt2-03-031921A). Because the sample material is detrital organic matter, and the source plant died before being incorporated into sediment, the ^{14}C age is a maximum limiting age for sediment deposition.

Optically Stimulated Luminescence. OSL thermochronometry was applied to terraces Qt9, Qt12 and Qt17 (samples QYt2-02-031921, QYt2-02-031921, QYt3-01-032121, Go-1, Go-3, and QDt-01-032121). OSL calculates sediment burial date by measuring the electrons in a quartz crystal lattice, having accumulated over the time that the quartz crystal was not exposed to light (Aitken, 1998). The viability of this technique depends on the assumption that channel sediment is exposed to light during transport, and then buried relatively rapidly, so that time since exposure to light would be an appropriate proxy for depositional age of the terrace. These samples were collected

following standard field procedures (Nelson et al., 2015), by inserting an eight-inch-long galvanized steel pipe into sediment exposure to extract sample preventing exposure to light.

Beryllium-10. ^{10}Be exposure dating was applied to terraces Qt12 and Q18 (samples VD-1 and VD-3). ^{10}Be reveals how long a sample has been exposed to the surface by measuring the amount of Beryllium-10 that has accumulated, through bombardment by cosmic rays, in quartz grains at or near Earth's surface (Gosse and Phillips, 2001). Fluvial sediment is assumed to be eroded from fresh or buried rock not previously exposed to the surface before fluvially transported and deposited along the channel bank. Upon deposition and floodplain abandonment, bombardment would begin. Samples were processed at the San Jose State University geochronology laboratory following standard mineral separation procedures and sample preparation (Gosse and Phillips, 2001).

Incision and Slip Rate Calculations

To determine incision rates of an elevated river terrace, three pieces of information must be known or estimated: (a) the elevation of the floodplain, or terrace surface, when the fluvial sediment was deposited, (b) the modern elevation of the surface, and (c) the time of abandonment of the channel. Precise floodplain elevation pre-abandonment cannot be known, so the elevation of the modern channel thalweg is used as an approximation. Laboratory ages are assumed to represent the time since the channel was abandoned, and rates are calculated by dividing the height of the terrace above the current streambed by the age of the sample.

Results from the point cloud analysis are used as values for heights above channel. All points, within the study area, that comprise a particular terrace are used to establish a range of elevations. This range encompasses, for a tilted terrace, the range of elevations on a tilted surface. The starting elevation before the terrace was uplifted is represented by the active channel elevation at downstream distance along Yager Creek (Figure 7). Age uncertainties are those reported by the laboratory. The elevation data are graphed in a scatter plot with axes ‘age’ versus ‘height above channel’ and include whiskers representing respective uncertainties (Figure 9) (e.g., Bender et al., 2016; Wesnowsky and Owen, 2020).

Slip rates were calculated for the GLF using two components: (a) vertical separation values of terrace surfaces and (b) age data. Cumulative vertical separation values are calculated using average separation values per terrace from each of the three strands. Cumulative separation values, for terraces which were also sampled for geochronology, are divided by average (where multiple) laboratory age, producing a rate in mm/yr.

RESULTS

Terrace Mapping and Analysis

I present new detailed mapping of fluvial terraces and streambeds in the vicinity of Hydesville, California, using one meter resolution lidar (Figure 4). I identified 229 individual terrace surfaces and interpreted 21 generations of deposition (terraces Qt0–Qt20) deposited by the Van Duzen River, Yager Creek, Wolverton Gulch, Wilson Creek, and Cuddleback Creek. I used ArcMap to calculate average slopes for each surface, which ranged from 1.0° to 8.6°, and to calculate aspect that was binned into 30° ranges. I present these data and observations in map (Figure 6) and tabular (Table 1*: Terrace observations based on Quaternary (Fig. 4) and slope-aspect (Fig. 6) maps. Observations are organized from broad to specific.*) formats.

I constructed a point cloud array of elevation data from selected terrace surfaces with respect to Yager Creek (Figure 7; also see Appendices A, B) using data from the DEM tied to the terrace mapping. Results from this point cloud show surface orientation relative to modern channel gradient, and revealed greater tilting and no surface offset in terraces Qt13W, and Qt14–Qt20, and lesser tilting plus three sets of surface offset in terraces Qt7–Qt12, Qt13C, and Qt13E. Qt13 was differentiated because its three segments (west, central, east) varied, across its five km span. The full point cloud contains over 32,000 elevation points and represents terrace surfaces relative to Yager Creek and the Van Duzen River.

Consistent with published mapping, I observed brown to black soil at the surface, up to two meters depth at field sampling sites. Outcrops stratigraphically below the soil were yellow to dark brown, poorly to well sorted, clay to cobble sized, and poorly to moderately consolidated sediment with clasts up to boulder size. Distinct gravel and cobble interbeds were up to one half meter thick and showed poorly constrained imbrication towards the north.

Structure Mapping and Analysis

Terrace mapping indicates three strands of the GLF (Figure 4) vertically separate multiple terrace surfaces. Fault traces of the GLF are not observed at the surface west of Wolverton Gulch, based on terrace mapping and point cloud analysis, and mapped as blind structures. I iteratively calculated vertical separations along three GLF strands at 100-, 150-, and 150-meter swatch widths for the south, central, northern strands, respectively. I selectively chose locations where correlative terraces were juxtaposed on either side. Values are plotted against along-strike fault distance with shaded annotation indicating terrace preservation (Figure 8). Vertical separation across the GLF ranges up to 9.5 meters per strand (Qt12, GLF central), and generally increases with terrace age (Figure 8).

Table 1: Terrace observations based on Quaternary (Fig. 4) and slope-aspect (Fig. 6) maps. Observations are organized from broad to specific.

Observation	Location	Terraces Affected	Description
1	NE of Y-VD confluence	All	Limited terrace preservation
2	S of Van Duzen River	All	Minimal terrace preservation observed
3	Van Duzen River	–	Active channel path is asymmetrically biased to south side of valley
4	NE of Y-VD confluence	Qt3, Qt16	Southside-up vertical separation along two WNW striking lineations
5	Study area	Qt7–Qt13E, Qt16	Southside-up vertical separation along 3 WNW striking lineations
6	Study area	Qt7–Qt13E	No consistent horizontal separation along 3 WNW striking lineations
7	Study area	Qt13W–Qt20 (minus Qt16)	No vertical separation observed
8	Study area	Qt7–Qt13E, Qt13C	Surface tilt ~1.5°–2.0°, generally oriented north to east, potentially progressive with age.
9	Study area	Qt13W–Qt20	Uniform surface tilt ~3.0°–5.0°, generally oriented north
10	Study area	Qt7–Qt12	Varied surface warping
11	Study area	Qt17–Qt19	Synclinal surface warping
12	Study area	Qt13W, Qt13C, Qt13E	Equivalent heights above channel along southern edge, and similar edge trajectory

Abbreviations and terminology: N=north, E=east, S=south, NE=northeast, WNW=west-northwest, Qt0–Qt20=terrace number, Qt13W=western Qt13 polygon, Qt13C=central Qt13 polygon, Qt13E=eastern Qt13 polygon Y=Yager creek, VD=Van Duzen River.

Geochronology

Ten samples were collected and analyzed from five different terraces (Figure 2) using ^{10}Be, OSL, and ^{14}C dating methods. The results of geochronological analyses are listed in Tables 2, 3, and 4, described in order of increasing age and organized by method.

Radiocarbon

Two charcoal fragments for ^{14}C age determination (QYt2-03-031921A, QYt2-03-031921R) (Table 2) were analyzed from bulk sediment collected at ~1.3 meters depth on terrace Qt7 from a hand-dug trench at a private residence at 40.54398° N, 124.074434° W. One sample charcoal fragment was rounded, and the other was angular. The latter is preferred because rounding is associated with transport and reworking. However, both samples yielded the same age. These samples show calibrated ages of cal yr B.P. 9530-9310 and 9460-9150, respectively.

Table 2: Radiocarbon ages and calibrated age ranges from terrace cover sediment, terrace Qt7, northwest of Yager Creek–Van Duzen River confluence.

Terrace Identifier	**Field sample number**	**Laboratory sample number[a]**	**Calibrated age range, years BP[b]**	**Lab-reported age[c]**	**Sample elevation (m); sample depth (m); sample location[d]**	**Material dated; stratigraphic context**
Qt7	QYt2-03-031921 Angular	PRI-6706 (UGAMS-53550)	9530–9310	8400 ± 30	87; 1.3–1.4; 40.5494, 124.0744	Charcoal–Cypress family (Cupressaceae); clayey silt below soil.
Qt7	QYt2-03-031921 Rounded	PRI-6725 (UGAMS-54514)	9460–9150	8320 ± 30	87; 1.3–1.4; 40.5494, 124.0744	Charcoal–Cypress family (Cupressaceae); clayey silt below soil.

[a] Samples were processed by the PaleoResearch Institute (PRI) following a modified Longin (1971) method of acid-base-acid chemical pre-treatment to remove non-native carbon contaminants.
[b] Calibrated age ranges (two standard deviations, 95.4%) reported as years BP (BP, before present), where 'present' is AD 1950. Calibrated ages calculated using OxCal (version 4.4.3, Bronk Ramsey, 2009; Bronk Ramsey and Lee, 2013; Reimer, 2013).
[c] Age reported in radiocarbon years at 68.2% precision, corrected for $\delta^{13}C$. Reported by the University of Georgia's Center for Applied Isotope Studies (UGAMS), using accelerator mass spectrometry in Athens, Georgia, USA.

Optically Stimulated Luminescence

OSL results indicate terrace ages increase with increasing height above the channel. Six total samples were analyzed using OSL (Table 3). Samples from Qt7 (QYt2-01-031921, QYt2-02-031921), collected at 1.3 and 1.5 meter depths, show 8760 ± 940 and 9670 ± 920 years since deposition, respectively. The above OSL age results for Qt7 overlap the two ^{14}C age results also for Qt 7. A roadcut was sampled at Qt9, at about one meter depth, and yielded an age of 20,000 ± 1000 years. Two samples were collected from Qt12 at 1.4- and 2.0-meter depth (Go1, Go-3) in a paleoseismic trench (Ladinsky, et al., 2020), and yielded OSL burial ages of 22,400 ± 2360 and 30,950 ± 2760 years ago. The younger age was on alluvial sediment nearer to the terrace surface and is therefore closer in age to the time that the Van Duzen River abandoned the Qt12 terrace. Qt17 was sampled at a road cut about three meters from the surface, (QDt-01-032121) and showed an OSL burial age of 38,250 ± 1920 years ago.

Table 3: Burial ages using optically stimulated luminescence (OSL) thermochronology for terrace cover sediment on terraces Qt9, Qt12, and Qt17, northwest of Yager Creek–Van Duzen River confluence.

Terrace Identifier	Lab Sample[d]	OSL age ± 1σ (ka)[e]	DE ± 1σ (Gy) [Age model]	No. of Aliquots[f]	Sample elevation (m); sample depth (m); sample location[d]	Geologic Setting
Qt7	QYt2-01-031921[g]	8.760 ± 9.40	8.56 ± 0.46 [MAM]	2 (26)	87, 1.3; 40.5494, 124.0744	Medium brown well sorted clayey silt
Qt7	QYt2-02-031921[g]	9.670 ± 9.20	8.81 ± 0.27 [MAM]	3 (25)	87, 1.50; 40.5494, 124.0744	Medium brown well sorted clayey silt
Qt9	QYt3-01-032121[g]	20.00 ± 1.00	36.6 ± 1.1 [MAM]	1 (29)	92, 1.0; 40.5468, 124.0810	Medium brown poorly indurated, poorly sorted conglomerate, fines to cobbles, clayey silty sand matrix
Qt12	Go-1[h]	22.40 ± 2.36	34.21 ± 4.63 [CAM][i]	16 (35)	102, 1.4; 40.5498, 124.0912	Dark brown to yellowish brown massive silt with very fine sand, trace rounded pebbles
Qt12	Go-3[h]	30.95 ± 2.76	57.52 ± 4.46 [CAM]	13 (35)	102, 2.0; 40.5498, 124.0912	Dark brown weakly indurated coarse sand to cobble gravel
Qt17	QDt-01-032121[g]	38.250 ± 1.920	61.3 ± 1.1 [MAM]	3 (21)	138, 3.0; 40.5559, 124.0910	Medium brown poorly indurated, slightly imbricated pebble to cobble gravel with silty to very fine sandy clay matrix

[d] Samples were collected following standard field procedures (Nelson et al., 2015).
[e] Samples were analyzed using single-aliquot regenerative-dose procedure on ≤1 mm quartz grains. OSL age and Equivalent dose (DE) calculated using the Central Age Model [CAM] or Minimum Age Model [MAM] of Galbraith and Roberts (2012).
[f] Number of replicated DE estimates used to calculate total equivalent dose. Figure in parentheses indicates total number of measurements included in calculating the represented DE and age.
[g] Analysis performed by USGS Luminescence Laboratory in Denver, Co following Gray et al. (2015) and Mahan and DeWitt (2019).
[h] Analysis performed by Utah State University Luminescence Laboratory, following Murray and Wintle (2000, 2003), Wintle and Murray (2006), Rhodes (2011), and Rittenour (2018).

Beryllium-10

^{10}Be was sampled on two surfaces at different heights and revealed a younger depositional age for the lower surface, closer to the channel, and an older age for the higher surface (Table 4). At Qt12, VD-3 revealed an exposure age of 23,954 ± 1839 years BP. At Qt18, VD-1 showed an exposure age of 46,334 ± 3570 years BP. Both samples were obtained from excavated pits and were the shallowest samples (10 cm depth) in a suite of samples that were originally obtained for ^{10}Be profile dating, but insufficient quartz at depth limited this approach, and motivated pursuing other geochronologic methods. The two samples each provide minimum-limiting ages.

Table 4: Beryllium-10 exposure ages (Gosse and Phillips, 2001) northwest of Yager Creek–Van Duzen River confluence. Table format after Levy and others (2018).

Terrace Identifier	**Lab sample[j]**	**^{10}Be Age ± Uncertainty (ka)[k]**	**Shielding Correction**	**Thickness (cm)**	**^{10}Be Concentration (atoms/g)**	**^{10}Be total measured error (1σ %)**	**Surface elevation (m); sample location**Error! Bookmark not defined.	**Lithology**
Qt12	VD-3	23.954 ± 1.839	1	10	89022	2.69	108; 40.5485, 124.0927	Volcanics
Qt18	VD-1	46.334 ± 3.570	1	10	191211	2.79	166; 40.5594, 124.0979	Volcanics

[j] Samples collected were a representative mixture of surface gravels.
[k] Ages reported by San Jose State University Geochronology Laboratory, San Jose, Ca. ^{10}Be/^{9}Be ratio for processing blank was 3.21E-16. Results represent a minimum age of the surface.

Incision and Slip Rates

Using depositional ages and heights above channel at sample sites, my results show the river incises, and terraces form, at about 2.3 to 5.2 mm/yr for the last ~47 ka (Table 5). Uncertainties for rate calculations had two dimensions: both age and height above terrace. Age uncertainty was produced by laboratory results. Height uncertainty was calculated based on terrace tilting. Terrace cover sediment should be the same age across a single terrace swath, but post depositional tilting creates a broad range of height values, and we cannot know a representative datum for terrace heights pre-tilting. Therefore, preferred rates use sample site heights, but I have also included rate ranges (Table 5) and whiskered data points (Figure 9) to address this uncertainty.

Table 5: Geochronology results from all samples (C14, OSL, ^{10}Be), and calculated incision rates, northwest of Yager Creek–Van Duzen River confluence. Further sampling details are tabularized per methodology in Tables 3–5.

Terrace Identifier	Lab Sample	Preferred incision Rate (mm/yr)[l]	Method	Age (yr)[m]	Sample height above channel (m)[n]	Terrace height range above channel (m)[n]	Rate range (mm/yr)[o]
Qt7	QYt2-03-031921R	**4.9–5.0**	^{14}C	9460–9150	45.9	37.5–57.5	4.0–6.3
Qt7	QYt2-03-031921A	**4.8–4.9**	^{14}C	9530–9310	45.9	37.5–57.5	3.9–6.2
Qt7	QYt2-01-031921	**5.2**	OSL	8760 ± 940	45.9	37.5–57.5	3.9–7.3
Qt7	QYt2-02-031921	**4.7**	OSL	9670 ± 920	45.9	37.5–57.5	3.5–6.6
Qt9	QYt3-01-032121	**3.0**	OSL	20000 ± 1000	59.1	37.0–79.1	1.8–4.2
Qt12	Go-1	**3.2**	OSL	22400 ± 2360	71.1	52.7–94.0	2.1–4.7
Qt12	VD-3	**3.1**	^{10}Be	23954 ± 1839	73.2	52.7–94.0	2.0–4.3
Qt12	Go-3	**2.3**	OSL	30950 ± 2760	71.1	52.7–94.0	1.6–3.3
Qt17	QDt-01-032121	**3.0**	OSL	38250 ± 1920	113.3	95.3–161.2	2.4–4.4
Qt18	VD-1	**3.2**	^{10}Be	46334 ± 3570	146.1	108.4–175.4	2.2–4.1

[l] Calculated using sample height above channel and laboratory age. ^{14}C laboratory results present an age range, whereas OSL and ^{10}Be laboratory results present a central age, and rate calculations here reflect this, further described in Results text.
[m] ^{14}C ages are before 1950, whereas OSL and ^{10}Be ages are before 2021.
[n] Calculated using elevation at sample location compared to modern thalweg elevation at lateral downstream distance.
[o] Calculated using full range of terrace height above channel and laboratory age range.

Using averaged depositional ages and cumulative vertical separation along the three strands of the GLF, my results show the GLF has slipped at a rate of 0.03–0.87 mm/yr (Table 6). Rates were calculated for terraces where both geochronology data was obtained, and vertical separation was observed: Qt7, Qt9, Qt12, Qt17.

Table 6: Slip rates based on vertical separation along the Goose Lake fault for south, central, and north strands. Separation values here are averages from data presented in Figure 8. Age values are averages from data presented in Tables 2–4.

Terrace identifier	**South strand (m)**	**Central strand (m)**	**North strand (m)**	**Cumulative separation (m)**	**Age (ka)**	**Slip rate (mm/yr)**
Qt3	0.4	1.7	–	2.0	–	**–**
Qt7	2.2	2.1	3.8	8.1	9.3	**0.87**
Qt8	2.2	3.9	–	6.1	–	**–**
Qt9	5.1	7.0	4.5	16.6	20	**0.83**
Qt10	8.4	–	–	8.4	–	**–**
Qt11	–	–	6.4	6.4	–	**–**
Qt12	7.6	5.8	1.0	14.4	26	**0.56**
Qt16	–	1.5	–	1.5	–	**–**
Qt17	–	–	1.2	1.2	38	**0.03**
Qt18	–	–	–	–	46	**–**

DISCUSSION

The findings of this investigation provide new insights about structure of the GLF, its deformation style, and constraints on activation history. In the following section, I discuss assumptions used in analysis, interpretations of results, and published works, in four parts: (i) terrace assignments to source channel, (ii) faulting history on the Goose Lake fault, (iii) a schematic kinematic model that addresses the Goose Lake fault tectonic setting, and (iv) uplift rates.

Terrace Assignments to Source Channel

Depositional channel assignments were important because they ultimately affected incision rate calculations. Terrace assignments were generally straightforward, with the exception of Qt2, Qt12, and Qt13E. These terraces were challenging because their shape and location did not clearly indicate a Van Duzen versus a Yager Creek source. These terraces were reasonably equidistant to both channels, and their shapes did not obviously mirror either channel (Figure 4). Furthermore, the general morphology of terraces northwest of the Yager–Van Duzen confluence indicates southeast migration: multiple terraces in that area have southeast facing front edges with ~90° corners which I interpret as ancestral confluence locations. I infer that both channels likely deposited sediment on each of these terraces at one point. However, based on back edge orientation, I assigned Qt2 and Qt13E as Van Duzen deposited, and Qt12 as Yager deposited.

Late Holocene History of Faulting on the Goose Lake Fault

Insights of faulting history in the last 46 ka were based on terrace chronology and tilting (Table 1), and vertical separation along the GLF (Figure 8). In general, a terrace slope that deviates from its original slope of formation can reveal deformation (e.g., McCalpin, 2009). The majority of terraces have north to east tilting slopes within the study area west of Yager Creek. Terrace tilting directions are at odds with the south Yager Creek gradient, the west Van Duzen River gradient, and the southeast migration of the Yager–Van Duzen confluence. Furthermore, older, and higher Van Duzen terraces, Qt13W–Qt20, have north tilted slopes of ~3.0°–5.0°, whereas younger, lower, mostly Yager terraces, Qt0–Qt13E, have north-to-east tilting slopes of ~1.5–2.0° (Figure 6). Importantly, these younger, flatter terraces also have been crosscut by surface traces of the GLF, but the older terraces have not. Based on these observations, I interpret that the central and southern strands of the GLF continue to the west as blind faults and are therefore responsible for higher angle tilting on the older, western terraces. For the northern strand, based on overall smaller separation values (maximum 6.5 m) and diminished separation values in Qt12 (<1 m), I infer (but with less certainty) that the northern strand also may continue as a blind fault further westward.

The varied gradient of Qt13 surfaces and the similar gradients of terraces older than Qt13 together may reveal time of inception of displacement on the GLF. Qt13 is mapped in three discrete surfaces–the largest, farthest west spans the town of Rohnerville (‘Qt13W’) (Qt13 locally is called the "Rohnerville terrace”), the central is relatively small and east adjacent (‘Qt13C’), and the third is to the east of Wolverton Gulch at the

southwest corner of Hydesville (‘Qt13E’) (Figure 4). The southern, front-edge heights and orientations of all Qt13 surfaces are very similar in height and trace, implying the same depositional age. Generally speaking, terraces (floodplains) deposited in the same vicinity and at the same time should form with the same original gradients. However, Qt13C and Qt13E show a lesser tilt, very similar to Qt7–Qt12, and Qt13W shows a greater tilt, more similar to Qt14–Qt20 (Figure 6). Based on this, I interpret that the GLF did not deform the surface until after Qt13 was deposited.

Evidence suggests that slip along the GLF must have begun after the deposition of Qt13, <38 ka. Qt13W through Qt20 appear to all have the same tilts (Figure 6). If faulting was active since the time of formation of Qt20, then the Qt13 to Qt20 terrace sequence would have progressively higher tilts with age, which they do not. Moreover, vertical separation across the GLF progressively increases from Qt7–Qt12 (Figure 8). The southern strand shows Qt12 and Qt10 with the greatest vertical separation, the central strand shows Qt12 with the greatest vertical separation (although the central strand also shows Qt12 vertical separation decreasing westward), and the northern strand shows Qt9 with the greatest vertical separation. Using terraces with the greatest vertical separation (Qt9 and Qt12) as a basis for fault initiation, the data presented here suggest a time bracket between Qt9 and Qt17, 20–38 ka. Although, since Qt9 and Qt12 are much closer in height compared to Qt17 (Figure 5), an estimate closer to 20 ka may be more appropriate.

Vertical separation along the GLF suggests the GLF has continued to slip at least as recently as post deposition of Qt7, ~9 ka (Figure 8, Table 6). Furthermore, because

terrace Qt7 is ~40 m above the modern channel, it is likely that multiple earthquakes have accommodated uplift of Qt7 to its present elevation. Also supporting recent slip on the GLF is the observation that two strands of the GLF mapped east of Yager Creek show vertical separation on Qt3.

Kinematic Model for Faulting Based on Terrace Deformation

Here I describe evidence to support a kinematic model for the GLF (Figure 10) and address contrasts from published interpretations. Older studies interpret two (McLaughlin et al., 2000) and three (Woodward-Clyde Consultants, 1980) strands of the GLF, and both studies map it as a north-dipping thrust. Paleoseismic trenching across the GLF central strand (Qt12) by Woodward-Clyde Consultants (1980) revealed north-dipping, high angle shearing, striations, and imbrication. They interpret that the GLF is north dipping, but with downwarping in the hanging wall which outpaces faulting, causing the hanging wall to be lower in elevation than the footwall. The schematic model of the GLF proposed by Woodward-Clyde Consultants (1980) suggests that the GLF is a bedding plane flexural-slip fault but is a rootless fault terminating near the surface (Appendix C). Woodward-Clyde Consultants (1980) do not explicitly account for the southern, nor northern, strands of the GLF in their model. Ladinsky and others (2020) trenched in a similar spot (at sample sites Go-1 and Go-3) and reaffirmed high angle shearing, and sub-vertical imbrication, and observed that the steeply dipping reverse fault was sub-parallel to steeply dipping bedding directly adjacent to the fault zone.

Other recent regional studies show evidence for active faulting in the subsurface. Verhey (2006) presented a north-south seismic reflection survey through the Eel River floodplain. The northern half of the 5.47 km-long seismic line is directly adjacent and parallel to Highway 101 and is one km west of the western edge of the study area (Appendix D). Therefore, inferred contacts from the seismic imaging can be projected eastward under the tilted Qt13 and older terraces. Verhey's (2006) interpretation of the seismic reflection line revealed southside-up offset (unidentified) stratigraphy. A south dipping blind detachment thrust fault explains offsets observed in the seismic data, as well as north-tilting Qt13–Qt20 within the study area of this thesis. Separately, Gordon (2009) presented a cross section of the east-west trending Grizzly Bluff anticline (Appendix E), 0.5 km southwest of the study area. Gordon similarly interprets multiple late-Pleistocene south-dipping reverse faults, based on industry well logs that show repeated units.

Furthermore, studies from faults with similar geometries can plausibly serve as models for the GLF. Lee and others (2001) investigated the Chelungpu fault after the 1999 Chi-Chi earthquake in Taiwan, and they interpreted a flower structure with surface faults dipping opposite the dominant thrust orientation. The surface profile of the Chelungpu fault shows a small scarp overriding a larger scarp oriented in the opposite direction; a profile very similar to the GLF central strand (Appendix F), and the GLF surface profile could be explained with the same subsurface geometry. Even more, north dipping faults (interpreted by Woodward-Clyde Consultants [1980]) near the surface may not preclude a dominant south dipping fault at further depth.

Elsewhere, Li and others (2017) showed terrace tilting can be caused by flexural slip with two models. The first, limb rotation, results in increased tilting angles in higher beds, closer to the hinge. The second, hinge migration, results in equivalent bed tilt angles. For my study, tilted terraces and regional compressional stress in this case may lead to this interpretation, but details make a flexural slip interpretation difficult to resolve. In my study site, younger terraces Qt7–Qt12 appear to follow a limb rotation model, where I find possible progressive tilt angles with age (although angles were too subtle to conclusively determine this). However, terraces Qt13W–Qt20 would appear to follow a hinge migration model based on equivalent tilt angles. Even if both models applied to this case (which Li and others [2017] do not describe as permissible) and the setting were to evolve from a limb rotation to a hinge migration model, the inconsistent tilting among Qt13W, Qt13C, and Qt13E make it highly unlikely.

My schematic model (Figure 10) of the GLF proposes kinematics for the GLF which satisfy the findings presented in this study. Findings of my research suggest that the GLF slipped multiple times from late Pleistocene to early Holocene, with differing kinematics to the east and west of Wolverton Gulch (Figure 10). I interpret that the GLF is a blind structure west of Wolverton Gulch, where terraces older than Qt13 tilt as a uniform block. Tilting in Qt13W Rohnerville terrace (3.0° N) calculated in this study is similar to the bedding dip (5° N) (Ogle, 1953), which indicates that the time-duration of tilting is generally confined to the age of that terrace, i.e., the last ~20–30 ka, based on dates presented here. Moreover, based on subsurface evidence (Verhey, 2006; Gordon, 2009), I interpret that the GLF at depth is the south-dipping reverse fault.

My interpretation of the GLF structure fits into the context of published regional mapping. Seismic epicenter data from Magee and others (1994) through the Humboldt Basin, illustrated in cross section by McLaughlin and others (2000), have mapped the GLF as a north dipping fault, but observed seismicity and geology do not preclude a south dipping interpretation. Epicenters are depicted at 4–6 km depth, and easily could be attributed to the south-dipping reverse fault Verhey (2006) suggests, which in turn could root in the high-angle south-dipping Russ fault (AppendicesAppendix G, Appendix H), as, while speculative, that is the closest major southern structure.

Channel Incision Rates as Uplift Rates

In the simplest model, incision rates of a fluvial system can be calculated using depositional ages of terrace surfaces and their heights above channel (e.g., McCalpin, 2009). However, many factors can affect elevation and therefore incision rates, including base level changes, active faults, and regional rock uplift. This section addresses possible influences on, and assumptions of, calculated uplift rates.

Eustatic sea level transgresses and regresses in cycles, which affect aggradation and incision for rivers which flow into the ocean. These uplift calculations, however, do not incorporate any possible effects of base level change. Mean sea level curves show cycles oscillate from high to low about every 100 ka, and the dataset of ~46–9 ka from this study falls within an overall regressive trend, although transgression accompanying ice sheet melting is characteristic of the time period since ca 14 ka (Lisiecki and Raymo, 2005). Regression trends could indicate a positive contribution to observed incision rates

relative to long term rates; as sea level drops, channel gradient works to equilibrate. I assume, however, that the ~23 river-km from the Van Duzen-Eel confluence to the ocean is likely too distal for base level to be measurably impacted by sea level change in the last 46 ka.

Comparing incision rates from this study to published regional rock uplift rates connects incision rates here to possible regional tectonic mechanisms. Previous studies focused on coastal marine terraces and used terrace uplift rates as a proxy for rock uplift rates via tectonic deformation ~100 km north of the study area, near Trinidad, CA (Padgett, 2019), and in the MTJ region (Merritts and Bull, 1989; Merritts and Vincent, 1989; Crawford, 2015; Hartshorn, 2017). Marine terraces near the Trinidad fault, ~70 km north of the MTJ (~41.1° N) which is the northernmost major fault within the SCSZ fold and thrust belt, show an average 0.5 mm/yr with a maximum of 1.0 mm/yr uplift in the last 125 ka. (Padgett, 2019). At a latitude equal to the MTJ (~40.4°–40.5° N), marine terraces at Bear River, Cape Ranch, and Singley Flat show maximum uplift rates of 3.25, 3.70, and 2.83 mm/yr, respectively (Hartshorn, 2017). Marine terraces have maximum uplift rates of 4.0 mm/yr ~33 km south of the MTJ (~40.3° N) at Randall Creek and decrease to 0.5 mm/yr farther south (Merritts and Bull, 1989). These results are consistent with interpretations that uplift rates are temporarily influenced by proximity to the MTJ as it migrates northward (Furlong and Govers, 1999; Furlong et al., 1989; Lock et al., 2006; Merritts and Bull, 1989).

Based on the similarly high uplift rates, and the proximity to the MTJ, paired with the relatively young depositional ages of terraces in this study, I interpret that incision

rates reflect rock uplift rates, and that the rock uplift is possibly connected to upper plate compressional faulting driven by the passage of the Mendocino triple junction. This study area is farther north and inland than previously documented study sites associated with the Mendocino triple junction, but this is the closest known regional driver for this type of deformation. It remains unknown, however, which upper plate structure(s) may be directly controlling the rapid rates documented here in the lower Van Duzen River valley.

Goose Lake Fault Slip Rates Within Context of Incision Rates

Slip rates calculated here for the Goose Lake fault establish a general understanding for the magnitude of slip of this particular fault and provide insight into how the GLF may relate to overall tectonic evolution of deformation in the lower Van Duzen River valley. Channel incision rates (maximum 5.2 mm/yr, Table 5) are an order of magnitude greater than GLF slip rates (0.03–0.87 mm/yr). This implies that there may be different drivers of channel incision; uplift from an underlying structure with significantly greater slip rate versus compression at a lesser rate along the GLF. It is unclear what structure(s) are directly driving deformation, and how they may relate. In Figure 10, I schematically propose the GLF structure at depth, but more research is needed to relate the GLF to the structure driving channel incision. Future work might include quantifying and comparing tilt on terraces west of Wolverton Gulch to vertical GLF slip on terraces east of Wolverton Gulch, age dating more terrace surfaces in the study area (Qt13, Qt7, Qt3) to refine slip history, age dating terraces in other areas of the

Humboldt basin to compare incision rates, and quantifying incision and GLF slip rates east of Yager Creek.

SUMMARY OF WORK

I interpreted twenty-one generations of fluvial terraces, deposited by the Van Duzen River, Yager Creek, Wolverton Gulch, Wilson Creek, and Cuddleback Creek, from 229 surfaces mapped on lidar DEMs in the Van Duzen River-Yager Creek confluence area.

I used ArcMap to analyze surface slope and aspect, which revealed older, higher Van Duzen-deposited terraces, Qt13W–Qt20, face north at ~3.0° to 5.0°, whereas younger, lower, mostly Yager-deposited terraces, Qt0–Qt13E, have north-to-east facing slopes of ~1.5° to 2.0°.

I interpret the Goose Lake fault has a significant southside-up vertical component of slip which ruptures the surface in three strands (south, central, north) east of Wolverton Gulch, and is concealed west of Wolverton Gulch, based on terrace mapping, elevation data, slope-aspect analysis, and subsurface data. These findings also suggest that the GLF dips north at the surface (at least, for the central strand, which was exposed in trench excavations), but south at depth. Geochronology data and vertical separation analysis indicate that the GLF slips at a rate of 0.03 to 0.87 mm/yr.

Incision rates of five terrace generations dated from 46 ka to 9 ka, based on ^{10}Be (n=2), OSL (n=7), and ^{14}C (n=2) analyses, range from 2.5 to 5.2 mm/yr. Based on these data, I infer that incision rates can be interpreted as regionally rapid long-term (late Pleistocene to present) rock uplift rates, greater than 2.5 mm/yr and as much as 5.2 mm/yr.

CONCLUSIONS

Findings from lidar terrace mapping and geochronological dating in this study reveal that the vicinity of the Yager Creek–Van Duzen River confluence has been actively uplifting at locally relatively high rates of 2.3 to 5.2 mm/yr over (at least) the past ~46 ka, likely driven by compressional upper plate faults and possibly associated with the migration of the Mendocino triple junction. Additionally, terraces have been deformed by ongoing slip of the Goose Lake fault, at a rate of 0.03 to 0.87 mm/yr, southside-up vertical offset, over the last ~38 to 9 ka. The GLF likely dips south at depth, expressing up to 16.6 m of total vertical separation at the surface east of the Wolverton Gulch, and is concealed as a blind fault system to the west of Wolverton Gulch. Based on GLF slip rates and channel incision rates that differ by an order of magnitude, I interpret that the dominant force driving these rapid incision rates is an underlying structure perhaps structurally related to, but nonetheless distinct from, the Goose Lake fault.

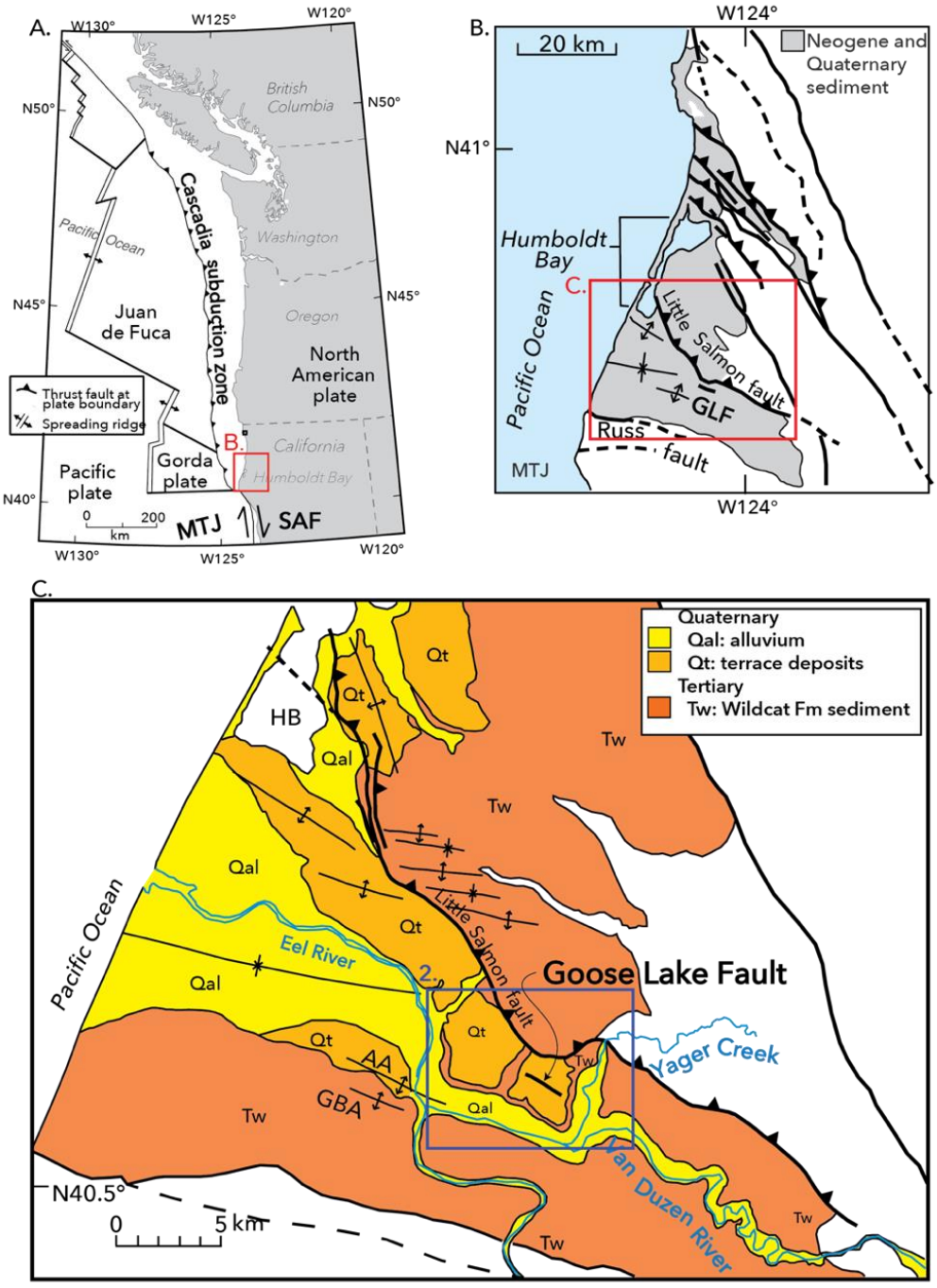

Figure 1: Overall setting of the study area. (A) Plate tectonic map of the Pacific northwest of North America. (B) Regional map showing selected faults and folds of northern California. (C) Simplified geologic map showing selected units near the study area. Abbreviations: MTJ=Mendocino triple junction, SAF=San Andreas fault, GLF=Goose Lake fault, HB=Humboldt Bay, AA=Alton anticline, GBA=Grizzly Bluff anticline. Modified from Ladinsky and others (2020).

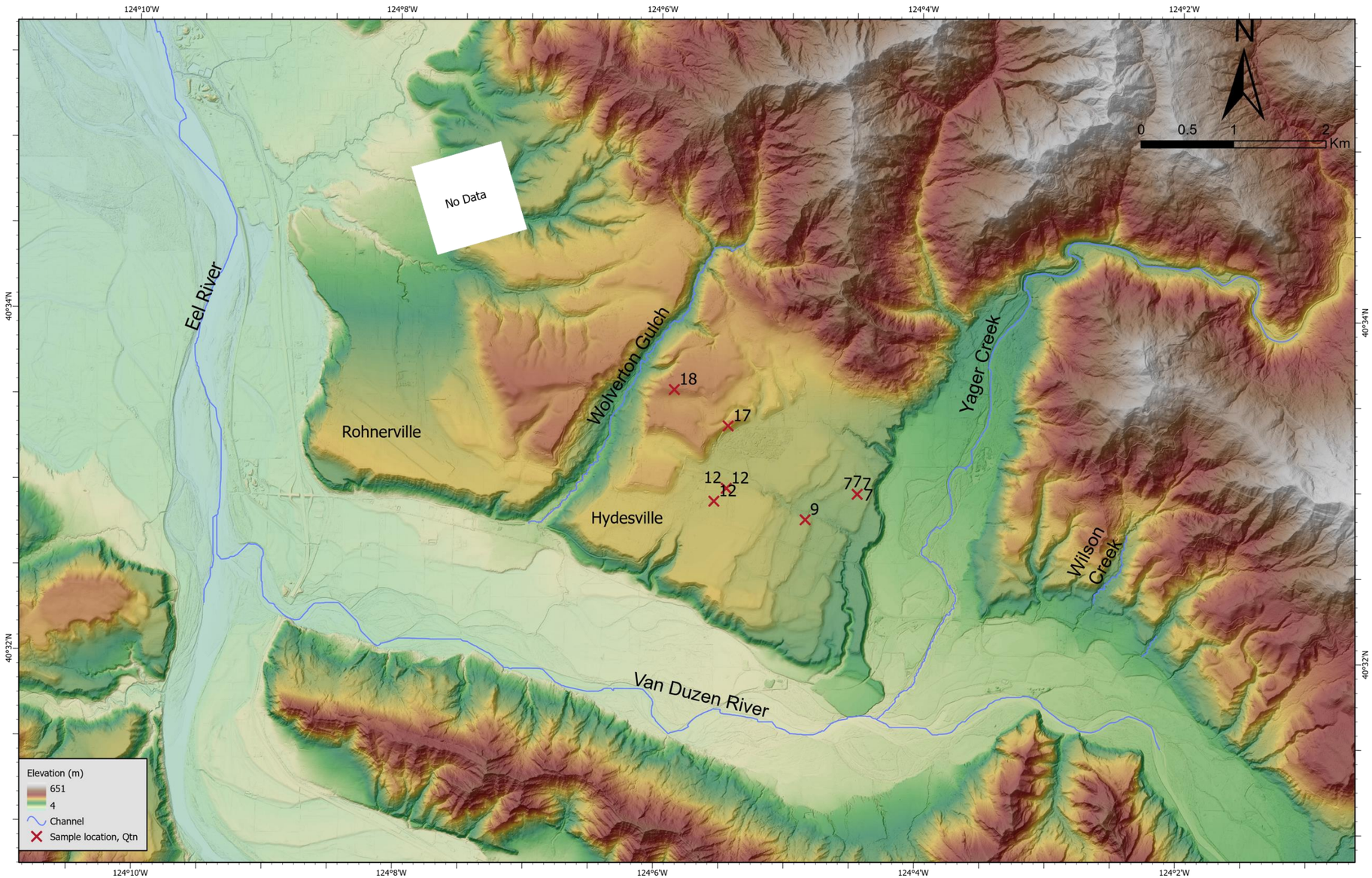

Figure 2: Bare Earth, shaded relief digital elevation model of the study area constructed with hill shade, slope shade, and elevation value raster layers. Placenames identify towns and stream channels, as marked. Numbered X locations identify sample sites for geochronology analysis; labels identify terrace number. Overall darker shades express lower elevations, higher slopes, and/or shadows. Data from USGS 1m lidar (2020), in NAD 1983 UTM Zone 10N and NAVD 1988 coordinate systems. Constructed in ArcGIS Pro.

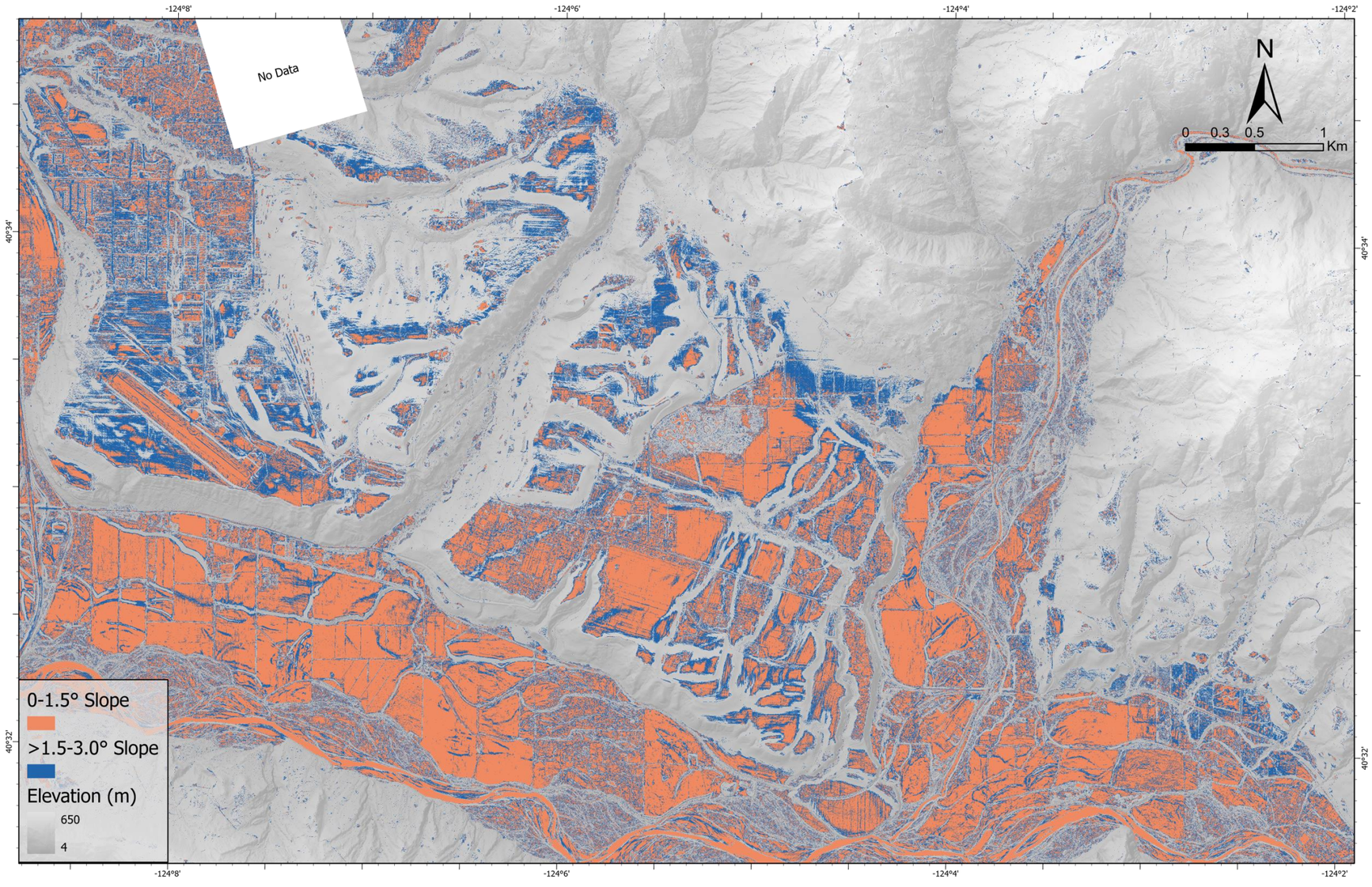

Figure 3: Shaded relief digital elevation model (DEM) with by stacked surface slope layers highlighting smooth, flat areas across the study area. Light orange shows areas with 0–1.5° slopes, and dark blue areas have >1.5–3.0° slopes. Terrace polygons were drawn based on these layers. DEM shows elevation, dark (low) to light (high), ranging from 4–651 m. Data from USGS 1m lidar. Constructed in ArcGIS Pro. Data from USGS 1m lidar (2020), using NAD 1983 UTM Zone 10N and NAVD 1988 coordinate systems. Constructed in ArcGIS Pro.

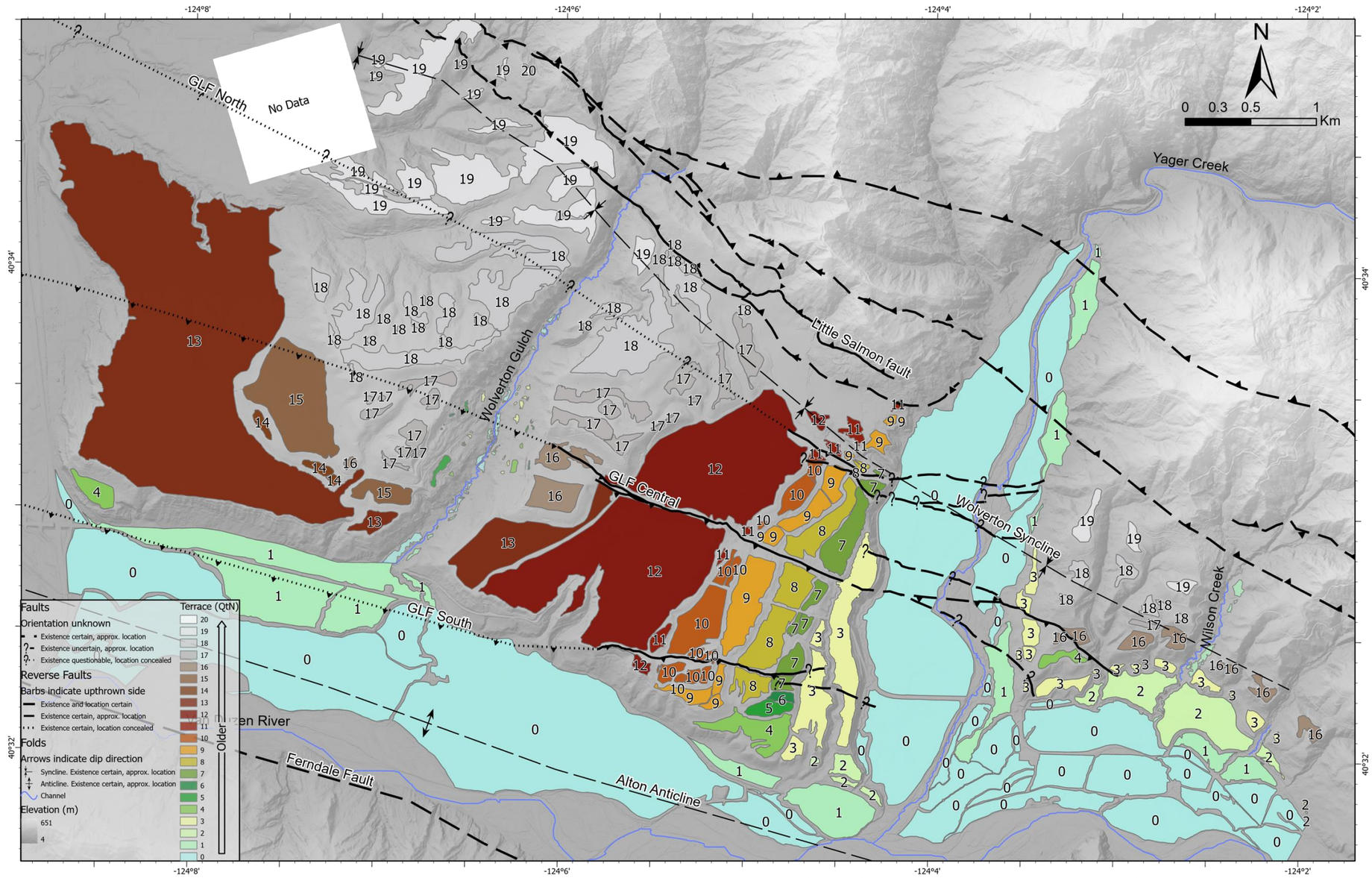

Figure 4: Map of fluvial terraces, faults, and streambeds overlaying DEM. Terrace numbers indicate relative depositional chronology. Polygons were delineated by maximum 3.0° surface slopes. Streambed lineations show thalweg, constructed using the ArcGIS Hydrology toolkit. Qt0 represents active floodplain adjacent to channels, and label numbers and shading denotes increasing age (Qt1–Qt20). DEM shows elevation, dark (low) to light (high), ranging from 4–651 m. Little Salmon fault, Ferndale fault, and Alton anticline were mapped based on the DEM and on Jennings (1994) and Ladinsky et al., 2020; USGS and CGS, 2020). Data from USGS 1m lidar (2020), using NAD 1983 UTM Zone 10N and NAVD 1988 coordinate systems. Constructed in ArcGIS Pro.

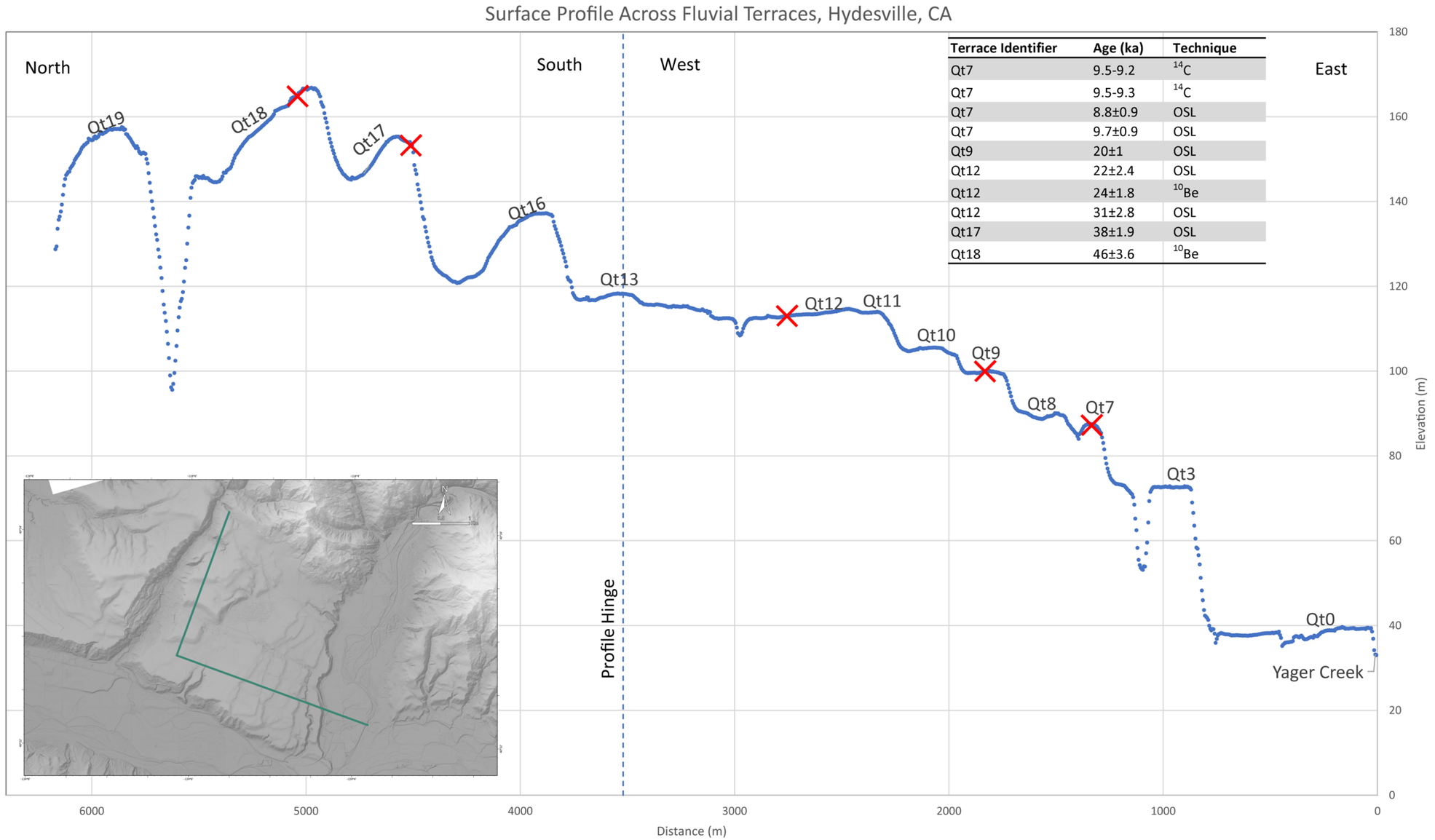

Terrace Identifier	Age (ka)	Technique
Qt7	9.5-9.2	^{14}C
Qt7	9.5-9.3	^{14}C
Qt7	8.8±0.9	OSL
Qt7	9.7±0.9	OSL
Qt9	20±1	OSL
Qt12	22±2.4	OSL
Qt12	24±1.8	^{10}Be
Qt12	31±2.8	OSL
Qt17	38±1.9	OSL
Qt18	46±3.6	^{10}Be

Figure 5: Surface profiles across fluvial terraces, location delineated in inset map. Terrace identifiers are labeled (Qtn), and equivalent sample locations are marked with red X (actual locations in Fig. 2). Age and sampling method are listed in table. From Yager Creek thalweg, profile projects westward, perpendicular to Yager Creek, then the profile projection rotates northward 90° at Qt13, orthogonal to the Van Duzen River. The higher, older terraces are projected from the Van Duzen perspective. Not all terraces are included since they were not observed along the projections. Data extracted in ArcGIS Pro from USGS (2020) 1m lidar, profile constructed in Microsoft Excel.

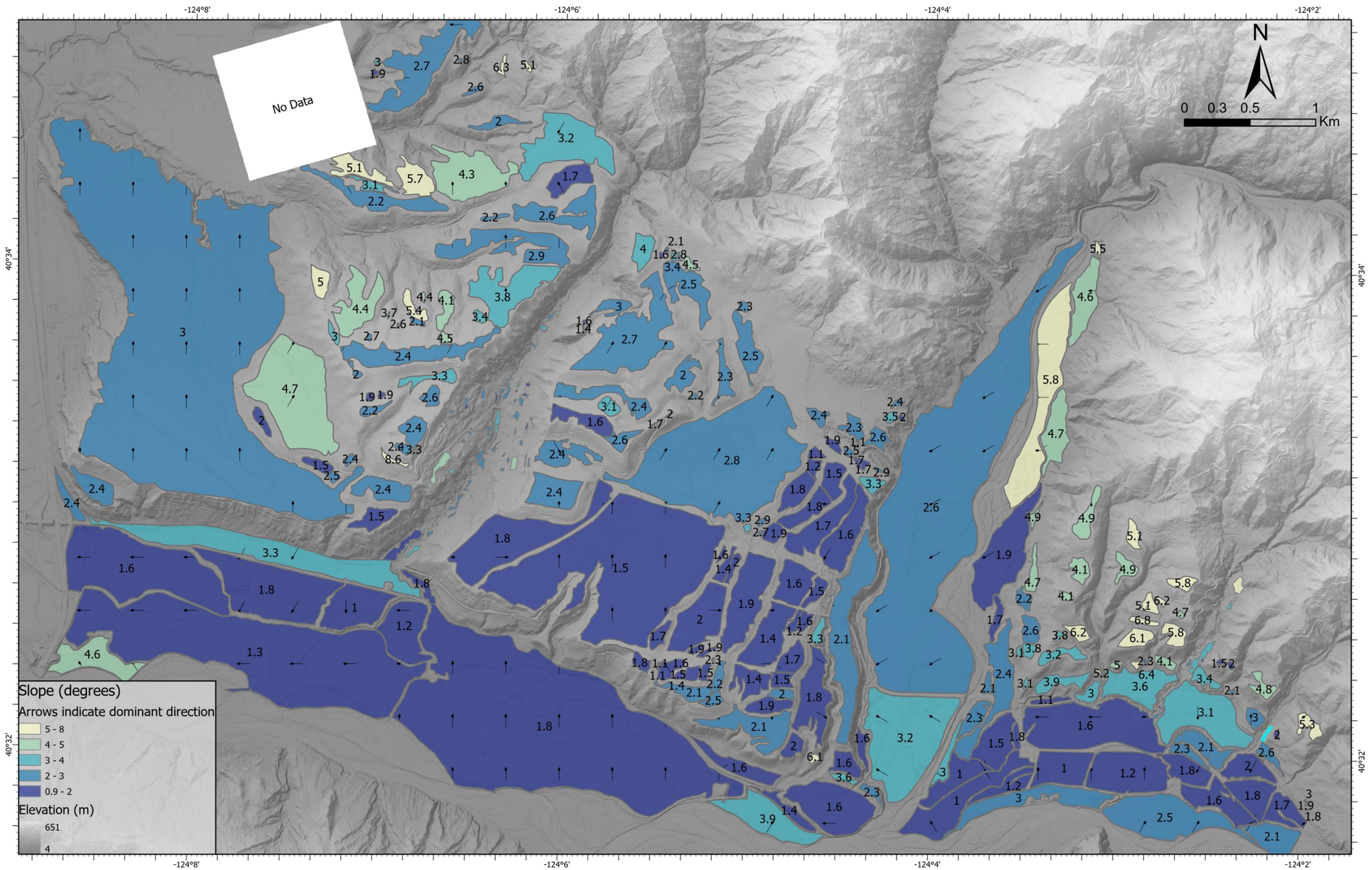

Figure 6: Slope aspect map of fluvial terraces overlaying DEM. Each polygon is annotated with average slope (degrees) and vectors, indicating dominant aspect. Polygon color gradient expresses increasing slope value, dark (low) to light (high). Aspects are binned into 12, 30° groups (N, NNE, ENE, E, ESE, SSE, S, SSW, WSW, W, WNW, NNW). Slope and aspect were analyzed using the ArcMap Slope and Aspect tools, respectively. DEM base layer shows elevation, dark (low) to light (high), ranging from 4–651 m. Data from USGS (2020) 1m lidar, using NAD 1983 UTM Zone 10N and NAVD 1988 coordinate systems. Constructed in ArcGIS Pro.

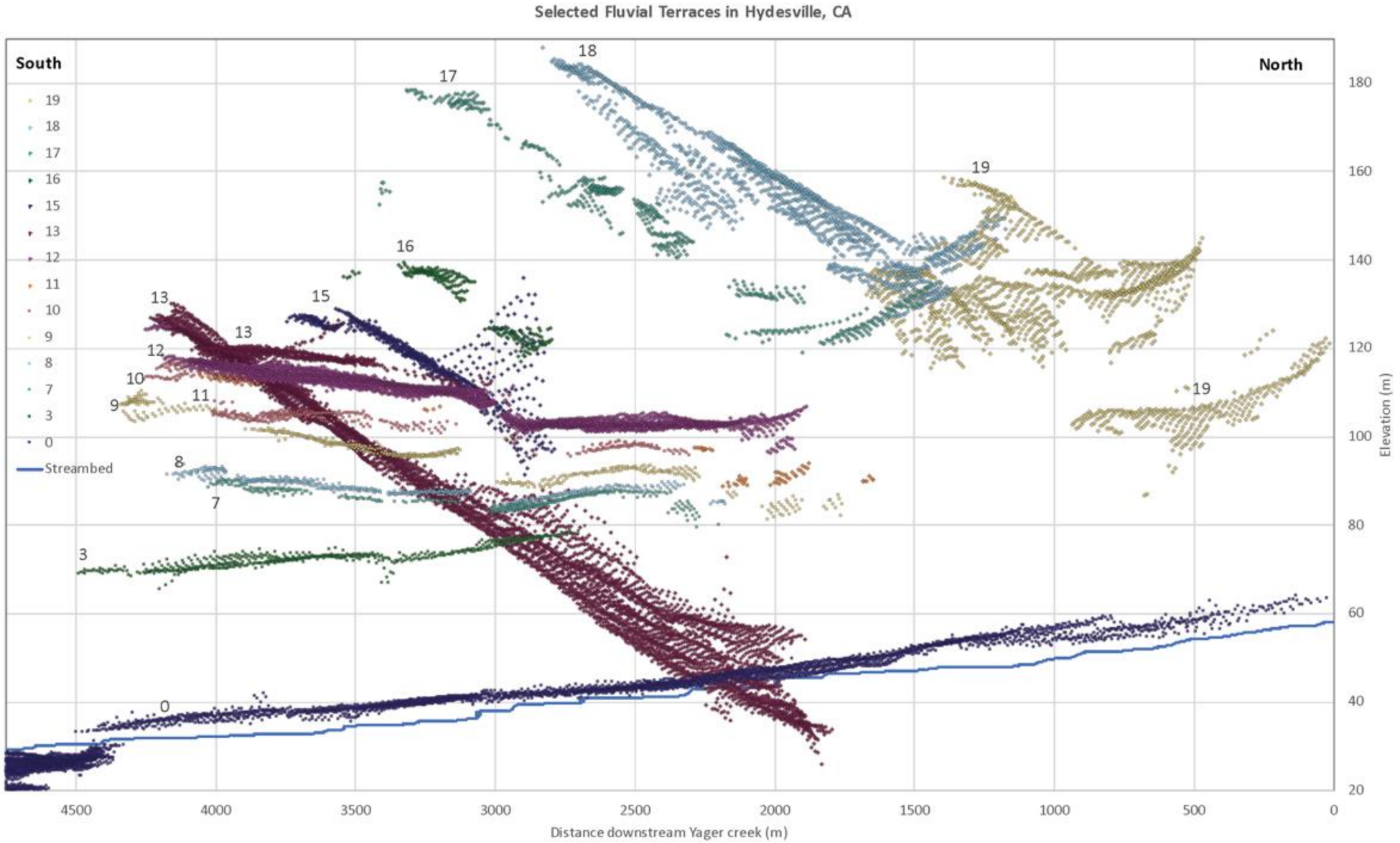

Figure 7: Point cloud of surface elevation values across selected terrace surfaces with respect to Yager Creek. Thalweg is lineated at base, with ascending terrace generations as marked. Values were plotted with respect to equivalent downstream distance to Yager Creek. Van Duzen River (not shown) flows westward at the south end (clustered Qt0 values represent Van Duzen floodplain, flowing into the page). Qt1, Qt2, Qt4, Qt5, Qt6, Qt11, and Qt20 had limited extents and were omitted for clarity. Values were extracted in a 25 by 25 m grid using Fishnet tool in ArcGIS Pro from USGS (2020) 1m lidar, and plotted in Microsoft Excel.

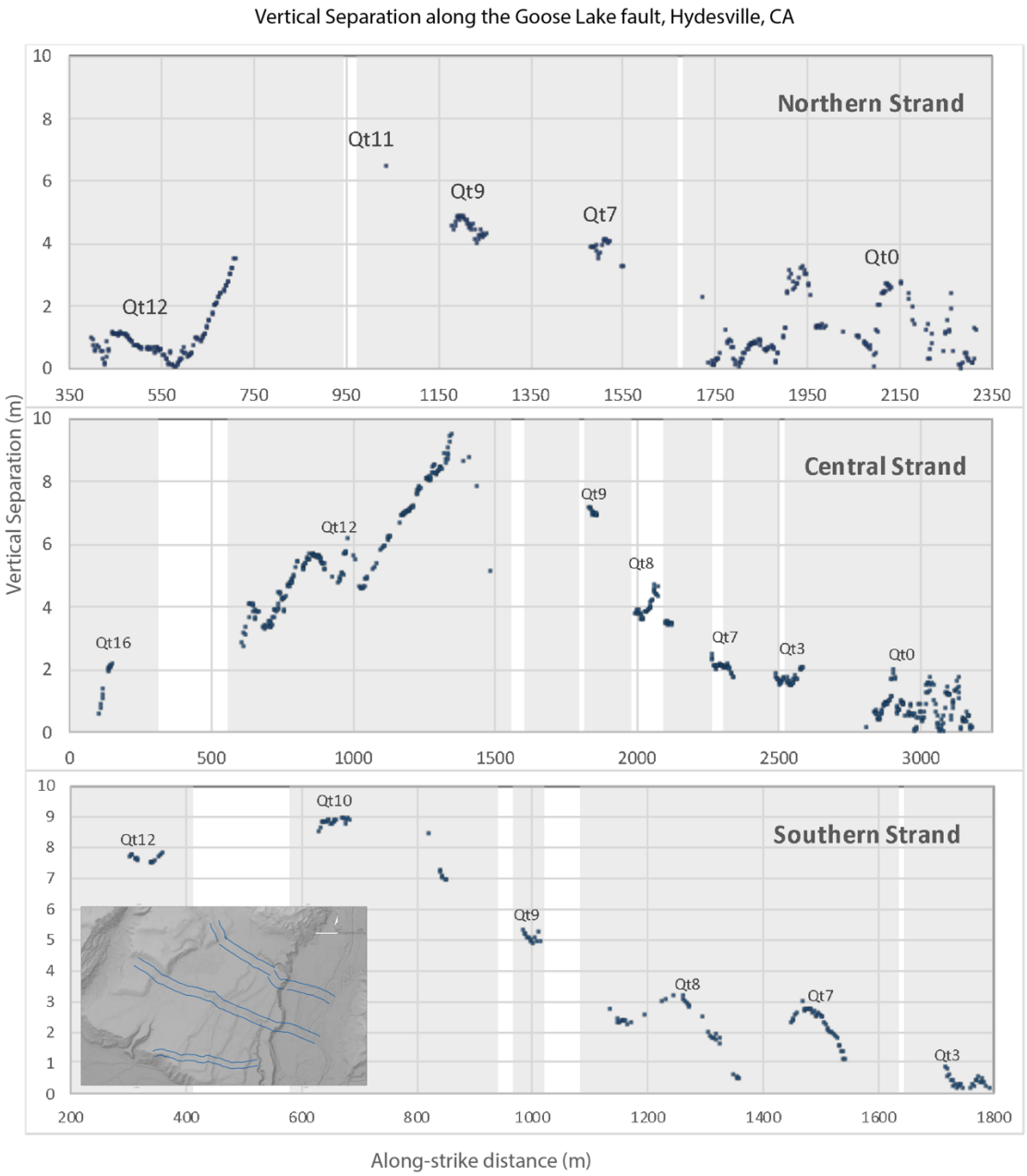

Figure 8: Vertical separation values across each strand of the Goose Lake fault are plotted in an along-strike direction from west to east. Gray shading indicates extent of terrace surfaces. Separation values were plotted for all points within surface polygons. Inset map shows corridors along which separations were measured.

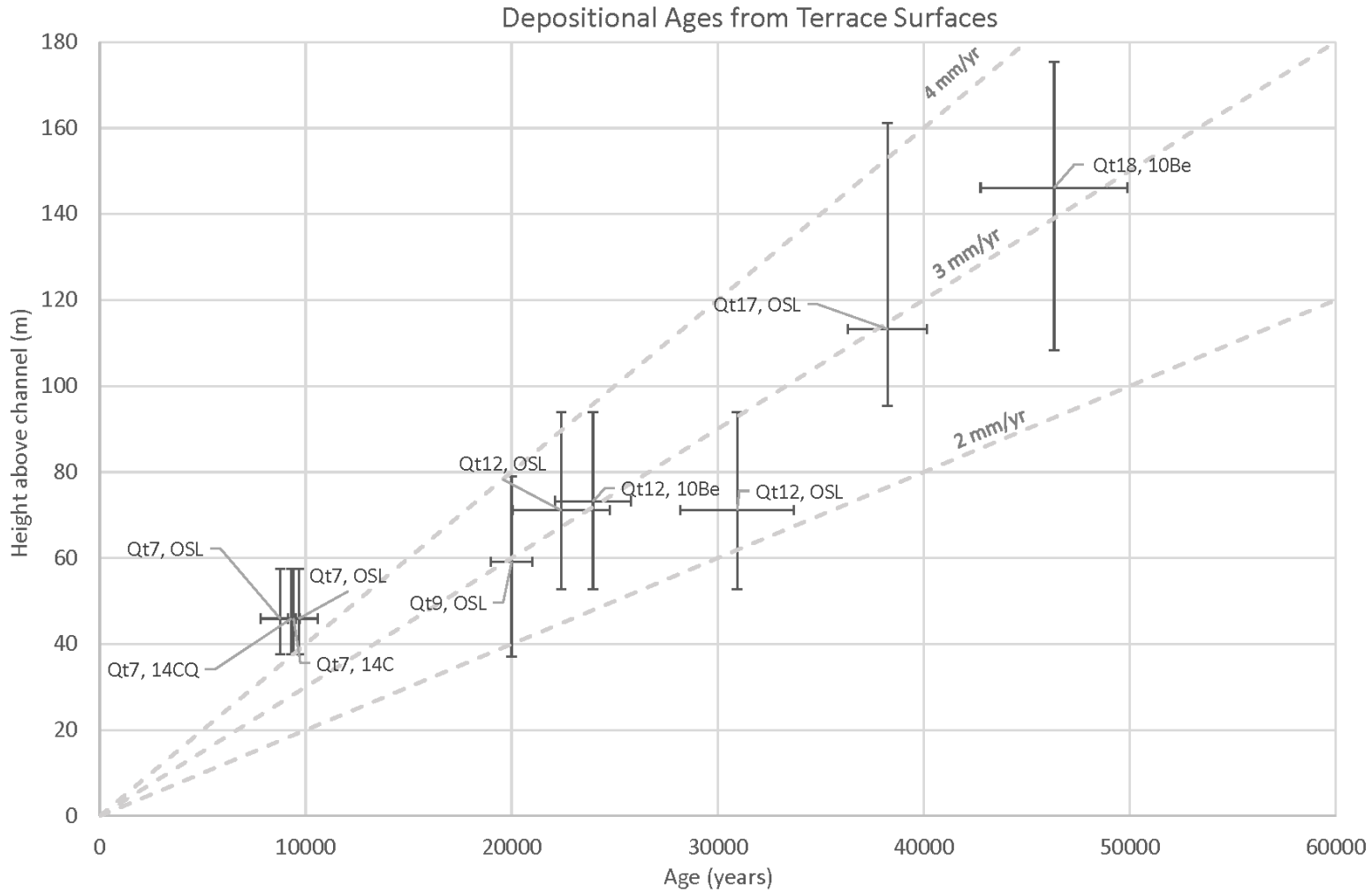

Figure 9: Ages for terrace surface plotted against height above channel. Horizontal whiskers indicate age uncertainty, and vertical whiskers indicate height range across the entire terrace. The height above the channel is based on a channel elevation defined by meters above active channel at downstream distance, as calculated using point cloud analysis (Fig. 7). Points are annotated with terrace identifier and method. Dashed lines are referential rates. Terrace heights were calculated using ArcMap with USGS 1m lidar, and plotted in Microsoft Excel.

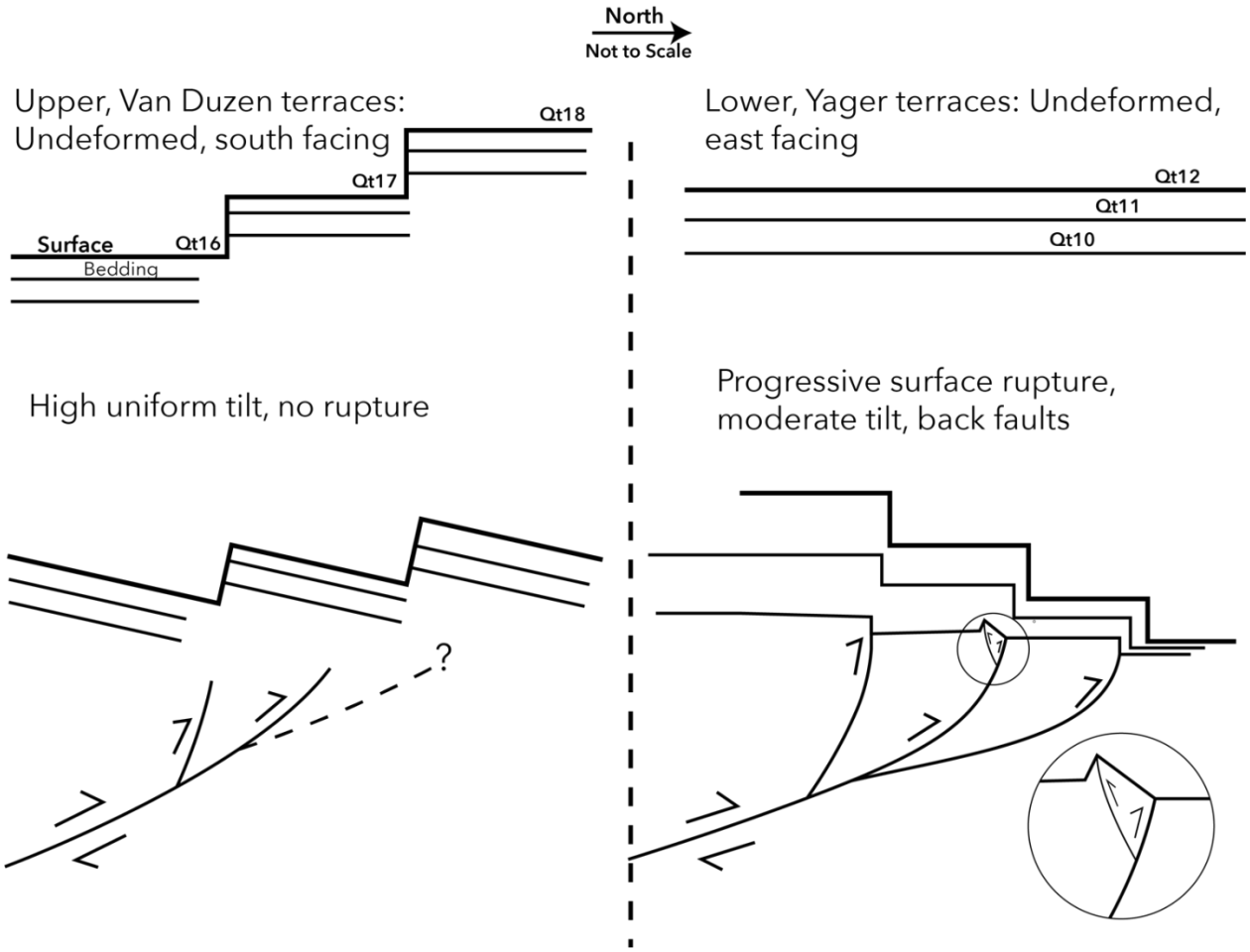

Figure 10: Schematic cross section model of the Goose Lake fault showing kinematics for blind faulting west of Wolverton Gulch (left), and southside-up faulting to the east (right). Upper images show terraces before faulting, lower images show deformed terraces, post-faulting. Note the stairstep morphology on the left side depicts south-facing terraces, whereas the right side shows progressive stairsteps created by faulting, as terraces face east (towards the reader).

REFERENCES

Aitken, M.J., 1998, Introduction to optical dating: the dating of Quaternary sediments by the use of photon-stimulated luminescence: New York, Oxford University Press, 106 p.

Anderson, R.S., and Anderson, S.P., 2011, Geomorphology: The mechanics and chemistry of landscapes: New York, Cambridge University Press, 651 p.

Atwater, T., 1970, Implications of plate tectonics for the Cenozoic tectonic evolution of western North America: Geological Society of America Bulletin, v. 81, p. 3513-3536, doi: 10.1130/0016-7606(1970)81[3513:IOPTFT]2.0.CO;2.

Bender, A.M., Amos, C.B., Bierman, P., Hood, D.H., Staich, Ll, Kelsey, H.M., Sherrod, B., 2016, Differential uplift and incision of the Yakima River terraces, central Washington State: Journal of Geophysical Research: Solid Earth, v. 121, 1, p. 365-384, doi: 10.1002/2015JB012303

Bronk Ramsey, C., 2009, Bayesian analysis of radiocarbon dates: Radiocarbon, v. 51(1), p. 337- 360, doi: 10.1017/S0033822200033865.

Bronk Ramsey, C., and Lee, S., 2013, Recent and Planned Developments of the Program OxCal: Radiocarbon, v. 55(2-3), p. 720-730, doi: 10.1017/S0033822200057878.

Carver, G. A., 1992, Late Cenozoic Tectonic Evolution of Coastal Northern California, in Field Guide to the Late Cenozoic Subduction Tectonics & Sedimentation of Northern Coastal California, *in* Field guide to the Late Cenozoic Subduction Tectonics & Sedimentation of Northern Coastal California, Gary A. Carver, Kenneth R. Alto: The Pacific Section American Association of Petroleum Geologists, v. GB 71, doi: 10.32375/1992-GB71.1.

Carver, G.A., and Burke, R. M., 1988, Trenching Investigations of Northwestern California Faults Humboldt Bay Region: National Earthquake Hazard Reduction Program Final Report: U.S. Geological Survey, p. 1-53.

Carver, G. A., Burke R.M., and Kelsey, H.M. 1986, Quaternary deformation in the region of the Mendocino triple junction: National Earthquake Hazard Reduction Program Final Report: U.S. Geological Survey, p. 1-48, doi: 10.1306/BDFF87AE-1718-11D7-8645000102C1865D.

Clarke, S.H., Jr., 1992, Geology of the Eel River Basin and adjacent region: Implications for Late Cenozoic tectonics of the Southern Cascadia subduction zone and Mendocino triple junction: American Association of Petroleum Geologists Bulletin, v. 76:2, p. 199-224.

Clarke, S.H., Jr., and Carver, G.A., 1992, Late Holocene tectonics and paleoseismicity, southern Cascadia subduction zone: Science, v. 255, p. 188-192, doi: 10.1126/science.255.5041.188.

Crawford, B., Geomorphic Map and Analysis of Uplifted Holocene Marine Terraces at the Southern Terminus of the Cascadia Subduction Zone: Cape Mendocino to Mouth of the Mattole River, Petrolia, CA, [Bachelor's thesis] Humboldt, California Polytechnic State University, 47 p.

Dengler, L., Moley, K., McPherson, R., Pasyanos, M., Dewey, J.W., Murray, M., 1995, The September 1, 1994, Mendocino Fault Earthquake: California Geology, v. 48(2), p. 43-53.

Furlong K.P., and Govers R., 1999, Ephemeral crustal thickening at a triple 525 junction: The Mendocino crustal conveyor: Geology, v. 27, no. 2, p. 127-130, doi: 10.1130/0091- 7613(1999)027<0127:ECTAAT>2.3.CO;2.

Furlong, K.P., Hugo, W.D., Zandt, G., 1989, Geometry and evolution of the San Andreas fault zone in northern California: Journal of Geophysical Research, v. 94 no. B3, p. 3100-3110, doi: 10.1029/JB094iB03p03100.

Furlong, Kevin P. and Susan Y. Schwartz, 2004, Influence of the Mendocino Triple Junction on the Tectonics of Coastal California: Annual Review of Earth and Planetary Sciences, v. 32, p. 403-433, doi: 10.1146/annurev.earth.32.101802.120252.

Galbraith, R.F., and Roberts, R.G., 2012, Statistical aspects of equivalent dose and error calculation and display in OSL dating: An overview and some recommendations, Quaternary Geochronology, v. 11, p. 1-27, doi: 10.1016/j.quageo.2012.04.020

Gavin, D. G., 2001, Estimation of inbuilt age in radiocarbon ages of soil charcoal for forest fire studies: Radiocarbon, v. 43, p. 27-44, doi: https://doi.org/10.1017/S003382220003160X

Gordon, G.S., 2009, Stratigraphic and sedimentologic controls on reservoir quality and distribution: Middle Wildcat Group, Grizzly Bluff gas field, Humboldt County, California [Master's thesis] Bakersfield, California State University, 118 p.

Gosse, J.C., and Phillips, F.M., 2001, Terrestrial in situ cosmogenic nuclides: theory and application: Quaternary Science Reviews, v. 20 (14), p. 1475-1560, doi: 10.1016/S0277-3791(00)00171-2.

Gray, H.J., Mahan, S.A., Rittenour, T.M., Nelson, M.S., 2015, Guide to luminescence dating techniques and their application for paleoseismic research: Proceedings volume: Basin and range province seismic hazards summit III: Salt Lake City, Utah Geological Survey Miscellaneous Publications 15-5, 18 p.

Hartshorn, E., 2017, Marine terrace formation associated with northern migration of the Mendocino triple junction uplift at Cape Mendocino, California [Bachelor's thesis] Humboldt, California Polytechnic State University, 55 p.

Kelsey, H.M, 2001, Active faulting associated with the southern Cascadia subduction zone in northern California: Division of Mines and Geology Bulletin, v. 210(12), p. 259-274.

Nicovich, S.R., 2015, Latest Pleistocene to Holocene river terrace deformation within the southernmost extent of the Little Salmon fault zone; geomorphic insights to fault termination and rupture history, Van Duzen River, northern California [Master's thesis] Humboldt, California Polytechnic State University, 97 p.

Hemphill-Haley, M. and Witter, R. C. 2006, Late Pleistocene paleoseismology of the southern Little Salmon fault, Strong's Creek, Fortune, California, Final Technical Report, National Earthquake Hazard Reduction Program, Award number 04HQGR004, 21 p.

Kelsey, H.M., and Carver, G.A., 1988, Late Neogene and Quaternary tectonics associated with northward growth of the San Andreas transform fault, northern California: Journal of Geophysical Research, v. 93, B5, p. 4797-4819, doi: 10.1029/JB093iB05p0479.

Levy, L.B., Kelly, M.A., Applegate, P.A., Howley, J.A., Virginia, R.A., 2018, Middle to late Holocene chronology of the southwestern margin of the Greenland Ice Sheet: a comparison with temperature records: Arctic, Antarctic and Alpine Research, vol. 50(1), doi: 10.1080/15230430.2017.1414477

Ladinsky, T. C., Kelsey, H. M., Michalak, M., 2020, In southern Cascadia, do upper plate faults rupture in concert with subduction zone earthquakes: a paleoseismic investigation of the Little Salmon Fault Zone, Final Technical Report, U.S. Geological Survey, National Earthquake Hazards Reduction Program, Award No. G19AP00045 & G19AP00046, 30 p.

Lavé, Jérôme, and Avouac, Jean-Philippe, 2000, Active folding of fluvial terraces across the Siwaliks Hills, Himalayas of central Nepal, Journal of Geophysical Research: Solid Earth, v. 105, B3, p. 5735-5770, doi:10.1029/1999JB900292.

Lee, J.C., Chen, Y.G., Sieh, K., Mueller, K., Chen, W.S., Chu, H.T., Chan, Y.C., Rubin, C., Yeats, R., 2001, A vertical exposure of the 1999 surface rupture of the Chelungpu fault at Wufeng, western Taiwan: structural and paleoseismic implications for an active thrust fault: Bulletin of the Seismological Society of America, v. 91 (5), p. 914-929.

Li, Tao, Chen, Jie, Jobe, Jessica A. Thompson, Burbank, Douglas W., 2017, Active Flexural-Slip Faulting: Controls Exerted by Stratigraphy, Geometry, and Fold Kinematics: Journal of Geophysical Research: Solid Earth, v. 122, no. 10, p. 8538-8565, doi: 10.1002/2017JB013966.

Lisiecki, L.E., and Raymo, M.E., 2005, A Plio-Pleistocene stack of 57 globally distributed benthic δ18O records: Paleoceanography, v. 20, 17 p., doi: 10.1029/2004PA001071.

Lock, J., Kelsey, H., Furlong, K., Woolace, A., 2006, Late Neogene and Quaternary landscape evolution of the northern California Coast Ranges: Evidence for Mendocino triple junction tectonics: Geological Society of America Bulletin, v. 118; no. 9-10, p. 1232-1246, doi: 10.1130/B25885.

Longin, R. 1971 New Method for Collagen Extraction for Radiocarbon Dating: Nature v. 230, p. 241-242.

Magee, M., McLaughlin, R.J., and Oppenheimer, D., 1994, Relationship of recent onshore and nearshore seismicity to the structural framework at the Mendocino Triple Junction [abs]: Geological Society of America Abstracts with Programs, v. 26, no. 7, p. A-146.

Mahan, S.A., and DeWitt, R., 2019, Principles and history of luminescence dating: Handbook of Luminescence Dating, Bateman, M.D. (ed.): Whittles Publishing, 416 p.

McCalpin, J., ed., 2009, Paleoseismology, International Geophysics Series, v. 95, 2nd edn.: Burlington, 613 p.

McCrory, P.A., 1995, Evolution of a trench-slope basin within the Cascadia subduction margin: the Neogene Humboldt Basin, California: Sedimentology, v. 42, p. 223-447.

McCrory, P. A., 2000. Upper plate contraction north of the migrating Mendocino triple junction, northern California: implications for strain partitioning: Tectonics, v. 19, no. 6, p. 1144-1160, doi: 10.1029/1999TC001177.

McLaughlin, R.J., Ellen, S.D., Blake, M.C., Jayko, A.S., Irwin, W.P., Aalto, K.R., Carver, G.A., and Clark, S.H., 2000, Geology of the Cape Mendocino, Eureka, Garberville, and Southwestern Part of the Hayfork 30 x 60 Minute Quadrangles and Adjacent Offshore Area, Northern California, U.S. Geological Survey, Miscellaneous Field Studies MF 2336.

McPherson, Robert C., 1992, Seismicity and stress at the southern end of the Cascadia subduction zone *in* Field Guide to the Late Cenozoic Subduction Tectonics & Sedimentation of Northern Coastal California, in Field guide to the Late Cenozoic Subduction Tectonics & Sedimentation of Northern Coastal California, Gary A. Carver, Kenneth R. Alto (eds): The Pacific Section American Association of Petroleum Geologists, v. GB 71, doi: 10.32375/1992-GB71.3.

Merritts, D. J., 1996, The Mendocino triple junction: Active faults, episodic coastal emergence, and rapid uplift: Journal of Geophysical Research, v. 101(B3): 6051-6070, doi: 10.1029/95JB01816.

Merritts, D.J., 2007, Fluvial environments, terrace sequences: Encyclopedia of Quaternary Science: Amsterdam, Elsevier, p. 694-704.

Merritts, D.J., and W.B. Bull, 1989, Interpreting Quaternary uplift rates at the Mendocino triple junction, northern California, from uplifted marine terraces: Geology, v. 17, issue 11, v. 17, p. 1020-1024, doi: 10.1130/0091-7613(1989)017<1020:IQURAT>2.3.CO;2.

Merritts, Dorothy, and Vincent, K.R., 1989, Geomorphic response of coastal streams to low, intermediate, and high rates of uplift, Mendocino triple junction region, northern California: Geological Society of America Bulletin, v. 100, p. 1373-1388, doi: 10.1130/0016-7606(1989)101<1373:GROCST>2.3.CO;2.

Molnar, P., 2004, Interactions among topographically induced elastic stress, static fatigue, and valley incision: Journal of Geophysical Research., v. 109, F02010, doi:10.1029/2003JF000097.

Murray, A.S., and Wintle, A.G., 2000, Luminescence dating of quartz using an improved single-aliquot regenerative-dose protocol: Radiation Measurements, v. 32 (1), p. 57-73, doi: 10.1016/S1350-4487(99)00253-X.

Murray, A.S., and Wintle, A.G., 2003, The single aliquot regenerative dose protocol: potential for improvements in reliability: Radiation Measurements, v. 37 (4-5), p. 377-381, doi: 10.1016/S1350-4487(03)00053-2

Nelson, M.S., Gray, H.J., Johnson, J.A., Rittenour, T.M., Feathers, J.K., Mahan, S.A., 2015, User guide for luminescence sampling in archaeological and geological contexts: Advances in Archaeological Practice, v. 3 (2), p. 166-177, doi: 10.7183/2326-3768.3.2.166.

Noaa Online Weather data (nowdata): Interactive Data Query System: Public Fact Sheet. Washington, D.C.: National Oceanic and Atmospheric Administration, accessed December, 2021, weather.gov/wrh/Climate?wfo=eka.

O'Dea, K. M., 1992, Terrace formation and deformation on Yager Creek, Humboldt County, California *in* A look at the southern end of the Cascadia subduction zone and the Mendocino triple junction, Friends of the Pleistocene, Pacific Cell, Field Guide, p. 229-234.

Ogle, B. A., 1953, Geology of the Eel River valley area, Humboldt County, California: Bulletin of the California Division of Mines, v. 164, 128 p.

Oppenheimer, D., Beroza, G., Carver, G, Dengler, L., Eaton, J., Gee, L., Gonzalez, F., Jayko, A., Li, W. H., Lisowski, M., Magee, M., Marshal, G., Murray, M., McPherson, R., Romanowicz,B., Satake, K., Simpson, R., Somerville, P., Stein, R., and Valentine, D., 1993, The Cape Mendocino, California, Earthquakes of April 1992: Subduction at the Triple Junction: Science, v.. 261, p. 433-437, doi: 10.1126/science.261.5120.433.

Padgett, J.S., Kelsey, H.M., Lamphear, D., 2019, Upper-plate deformation of late Pleistocene marine terraces in the Trinidad, California, coastal area, southern Cascadia subduction zone: Geosphere, v. 15, doi: 10.1130/GES02032.1.

Patton, Jay, 2021, Tectonic Terraces at the Triple Junction: Geological Society of America Abstracts with Programs, v. 53, no. 6, doi: 10.1130/abs/2021AM-366769.

Reimer, P. J. and 29 others, 2013, Intcal 13 and Marine 13 radiocarbon age calibration curves 0–50,000 years cal BP: Radiocarbon, v. 55, no. 4, p. 1869–1887.

Rhodes, E.J., 2011, Optically stimulated luminescence dating of sediments over the past 200,000 years: Annual Review of Earth and Planetary Sciences, v. 39, p. 461-488, doi: 10.1146/annurev-earth-040610-133425.

Rittenour, T.M., 2018, Dates and Rates of Earth- Surface Processes Revealed using Luminescence Dating: Elements, v. 14 (1), p. 21-26, doi: 10.2138/gselements.14.1.21.

Robinson, M.L., 2016, Terrace formation in the upper headwater region of the Mattole river watershed across the Mendocino triple junction, northwest California [Master's thesis] Humboldt, California Polytechnic State University, 71 p.

Rollins, John C., and Stein, Ross S., 2010, Coulomb stress interactions among M≥5.9 earthquakes in the Gorda deformation zone and on the Mendocino Fracture Zone, Cascadia megathrust, and northern San Andreas fault: Journal of Geophysical Research: Solid Earth, v. 115, B12306, p. 1-19, doi:10.1029/2009JB007117.

Stallman, J.D., 2003. Strath Terrace Genesis in the North Fork Elk River Valley, North Coastal California, [Master's thesis]: Humboldt, California Polytechnic State University, 104 p.

U.S. Geological Survey, The National Map, 3DEP products and services: The National Map, 3D Elevation Program Web page: nationalmap.gov/3DEP/3dep_prodserv.html accessed January, 2020.

U.S. Geological Survey and California Geological Survey, Quaternary fault and fold database for the United States, accessed February 1, 2020, at: usgs.gov/natural-hazards/earthquake-hazards/faults.

Verhey, M., Subsurface seismic reflection in the Van Duzen/Eel River Valley, 2006, *in* Signatures of Quaternary crustal deformation and landscape evolution in the Mendocino deformation zone, NW California, Simpson, G. D., Roberts, M.A.: Friends of the Pleistocene field guide, p. 111-114.

Vadurro, G. A., Bickner, F. R., Lindberg, D. N., Manhart, G. L., and Watt, C. J., 2006, Fault Surface Rupture and Fold Hazard Evaluation of the Little Salmon Fault at the College of the Redwoods Eureka Campus, Southern Cascadia Subduction Zone Fold and Thrust Belt, NW California *in* Signatures of Quaternary crustal deformation and landscape Evolution in the Mendocino deformation zone, NW California, Simpson, G. D., Roberts, M.A.: Friends of the Pleistocene field guide, p. 121-136.

Wells, Ray E., Weaver, Craig S., Blakely, Richard J., 1998, Fore-arc migration in Cascadia and its neotectonic significance: Geology, v. 26, no. 8, p. 759-762, doi: 10.1130/0091-7613(1998)026<0759:FAMICA>2.3.CO;2.

Wesnousky, S.G., and Owen, L.A., 2020, Development of the Truckee River terraces on the northeastern flank of the Sierra Nevada: Geomorphology, v. 370, 11 p., doi: 10.1016/j.geomorph.2020.107399.

Williams, T. B., Kelsey, H. M. and Freymueller, J.T., 2006, GPS-derived strain in northwestern California: Termination of the San Andreas fault system and convergence of the Sierra Nevada-Great Valley block contribute to southern Cascadia forearc contraction: Tectonophysics, v. 413, no. 3-4, p.171-184, doi: 10.1016/j.tecto.2005.10.047.

Wintle, A.G., and Murray, A.S., 2006, A review of quartz optically stimulated luminescence characteristics and their relevance in single-aliquot regeneration dating protocols: Radiation Measurements, v. 41 (4), p. 369-391, doi: 10.1016/j.radmeas.2005.11.001.

Witter, R.C., Patton, J.R., Carver, G.A., Kelsey, H.M., Garrison-Laney, C., Koehler, R.D., and Hemphill-Haley, E., 2002, Upper plate earthquakes on the western Little Salmon fault and contemporaneous subsidence of southern Humboldt Bay over the past 3,600 years, northwestern California, U.S. Geological Survey, National Earthquake Hazard Reduction Program Final Technical Report, Award number 01HQGR0125, 44 p.

Woodward-Clyde Consultants, 1980, Evaluation of the potential for resolving the geologic and seismic issues at Humboldt Bay Power Plant Unit Number 3, Appendices A, B and C: Technical report to Pacific Gas and Electric Company, Walnut Creek, California.

APPENDICES

Appendix A: Point cloud of surface elevation values across all terrace surfaces northwest of Yager Creek–Van Duzen River confluence, from Yager Creek perspective.

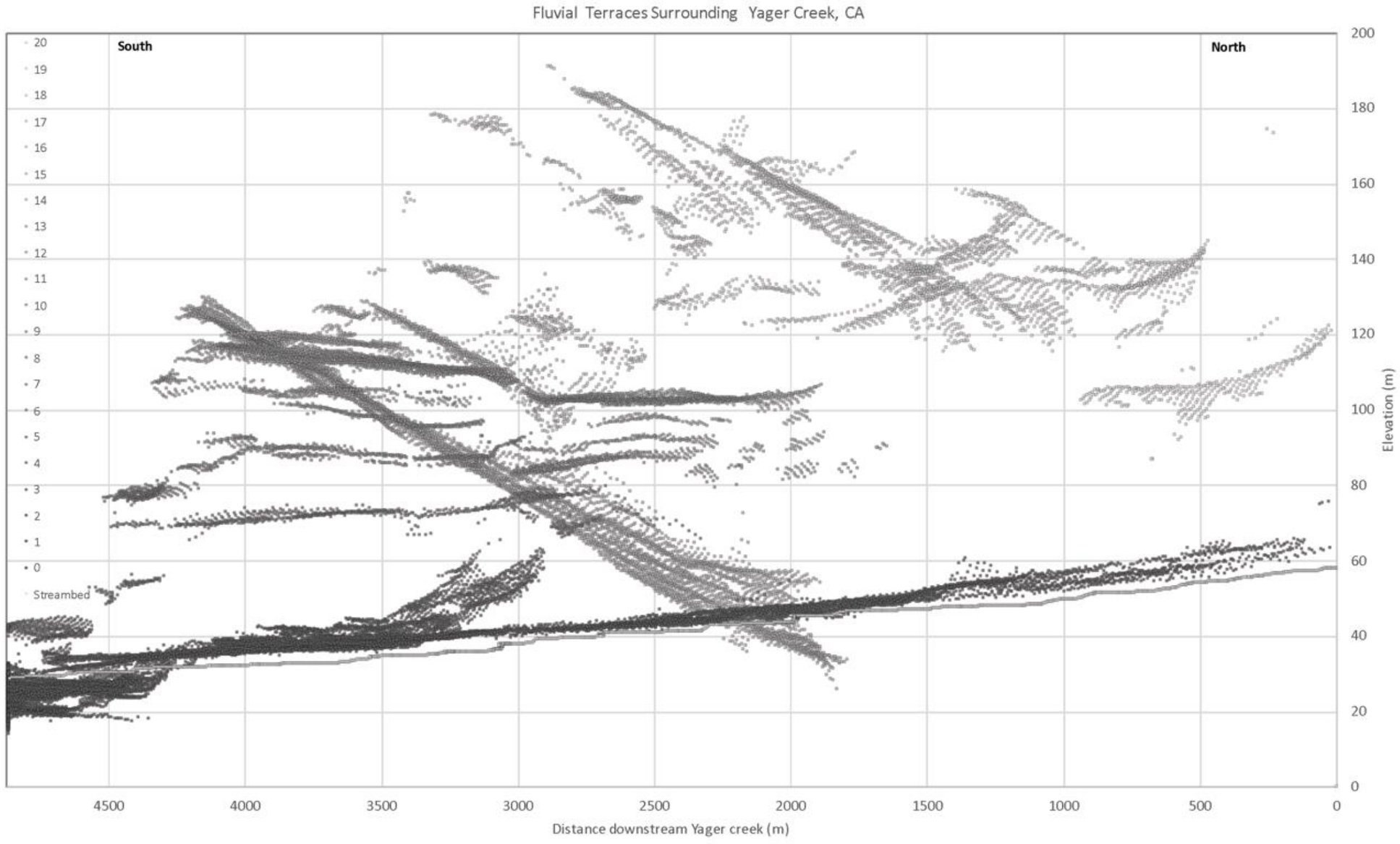

Appendix B: Point cloud of surface elevation values across all terrace surfaces northwest of Yager Creek–Van Duzen River confluence, from Van Duzen River perspective. Zero distance is at Van Duzen–Eel River confluence.

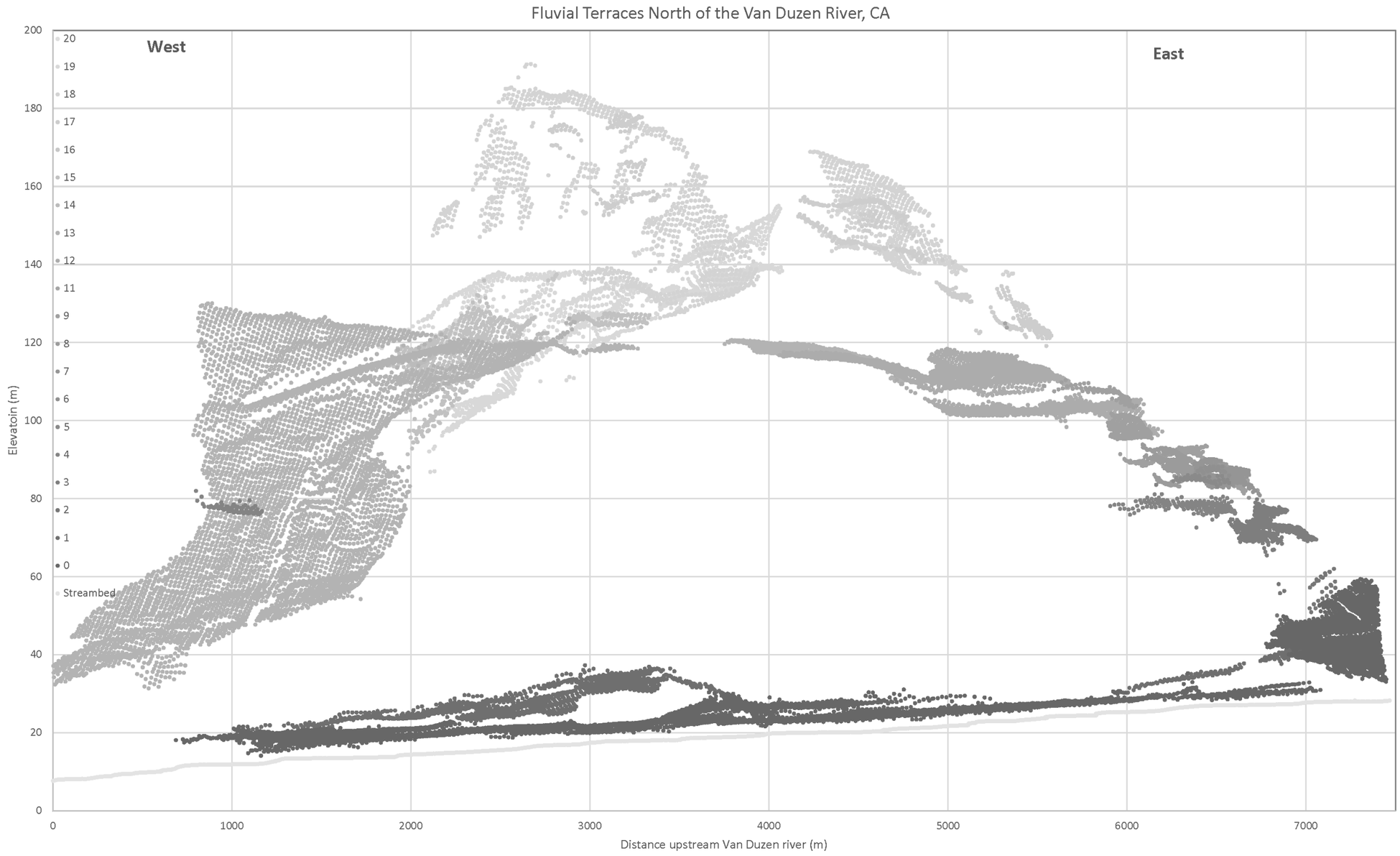

Appendix C: Alternative model for study area by previous researchers. Schematic north-south cross section showing Little Salmon fault and Goose Lake fault. Rate of synclinal downwarping is assumed to exceed rate of slip on Goose Lake fault. From Woodward-Clyde Consultants (1980)

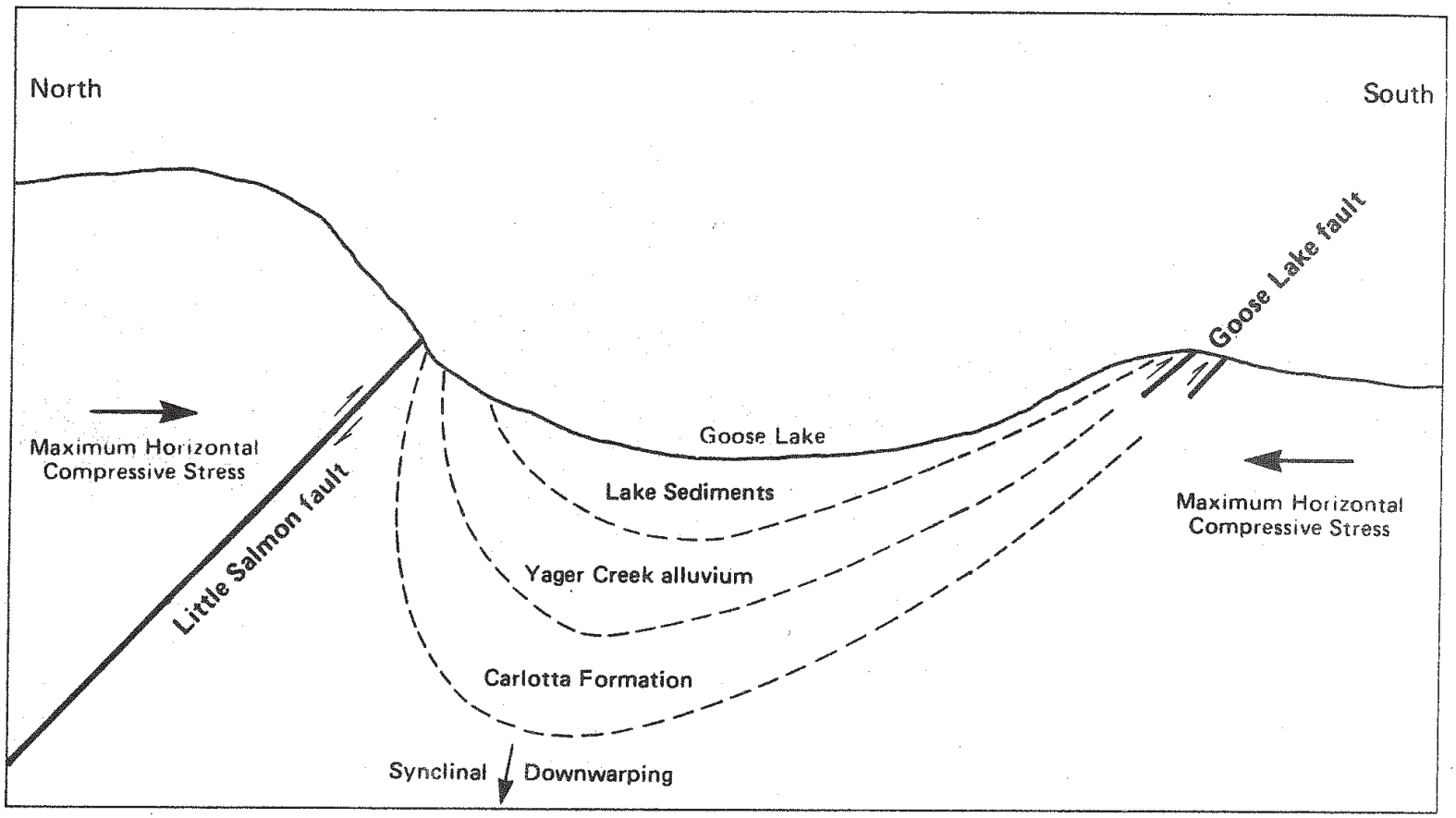

Appendix D: Industry seismic reflection line shown at depth, and in map view with interpretations by Verhey. Profile crosses the Grizzly Bluff anticline (GBA). Basemap with Neogene stratigraphy (Ogle, 1953) draped over USGS 10 M digital elevation model shaded relief mosaic. Basemap DEM image and geologic map overlay: T. Leroy. Modified from Verhey (2006).

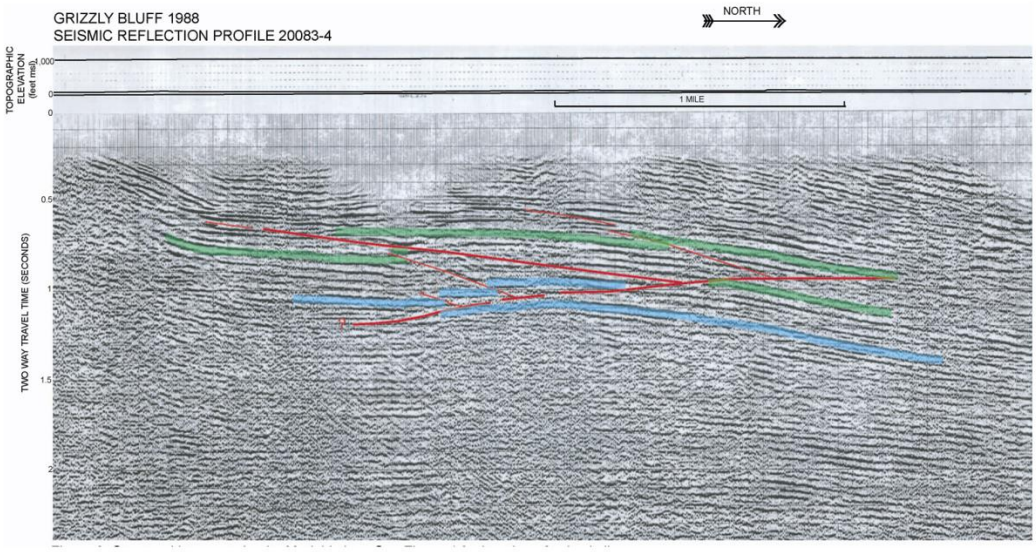

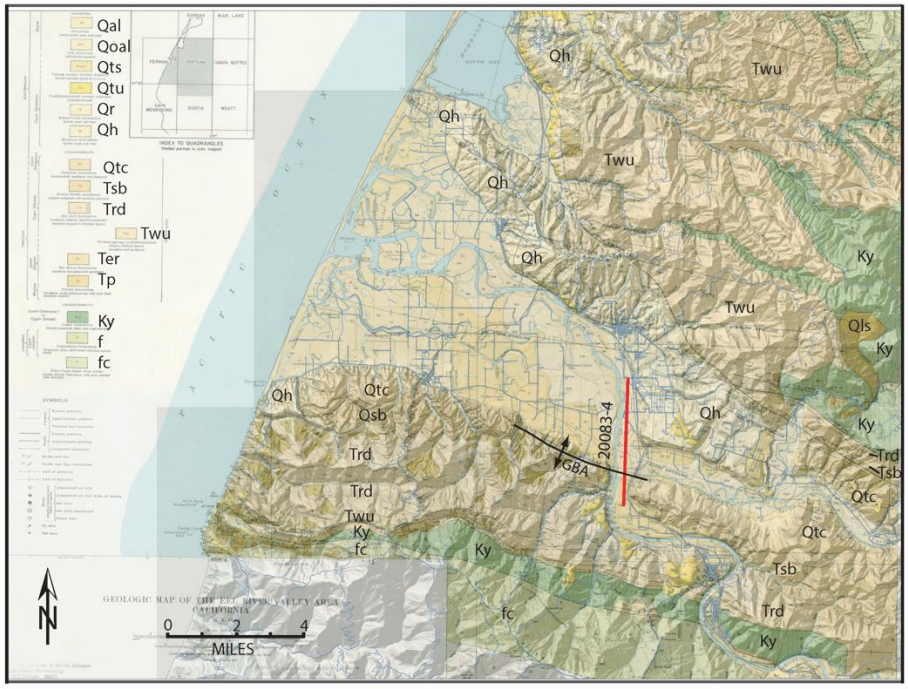

Appendix E: North-south interpretive geologic cross section north of the Russ fault, crossing the Grizzly Bluff anticline, along the Eel River valley, west of the study area. Constructed using well log data. Modified from Gordon (2009).

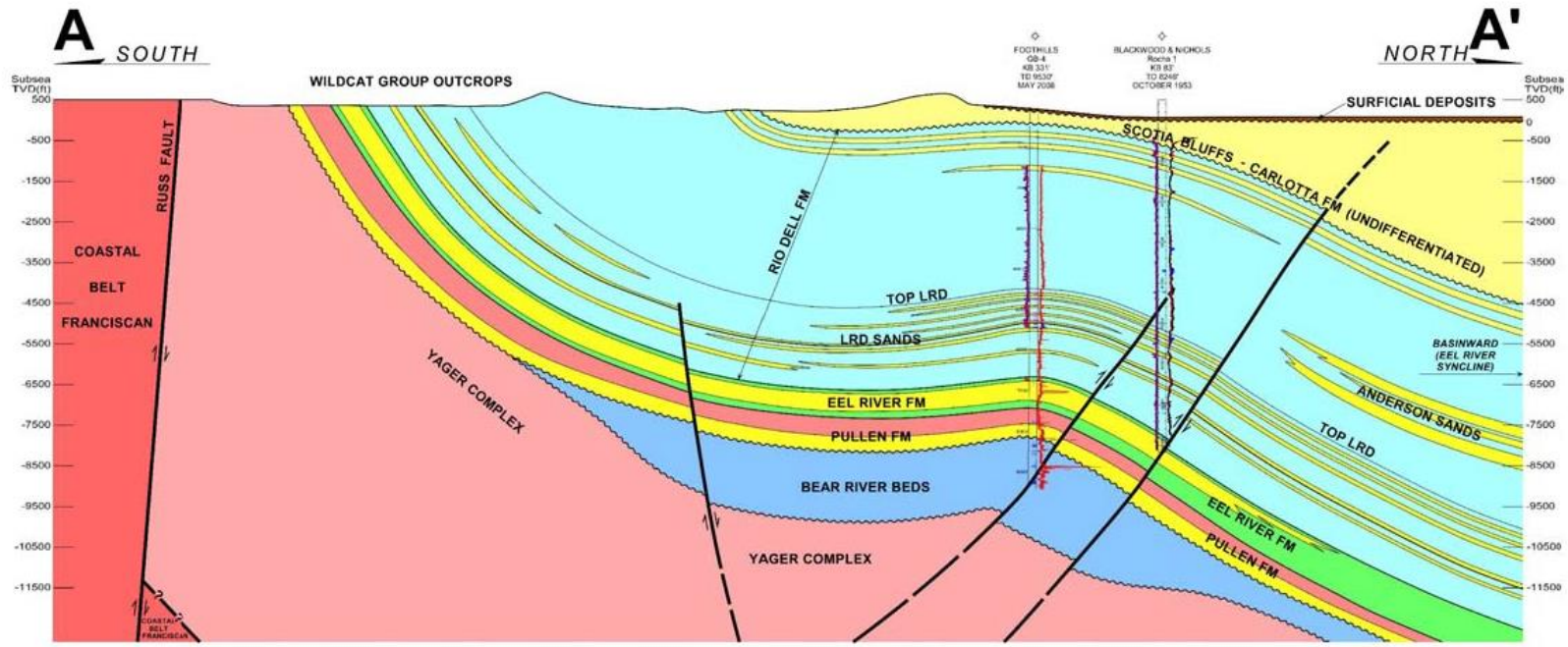

Appendix F: A and B show interpretive paleoseismic trench logs of the Chelungpu thrust fault in Taiwan after the 1999 Chi-Chi earthquake modified from Lee and others (2001). For comparison, interpretive paleoseismic east trench wall log (C), and surface profile (D)

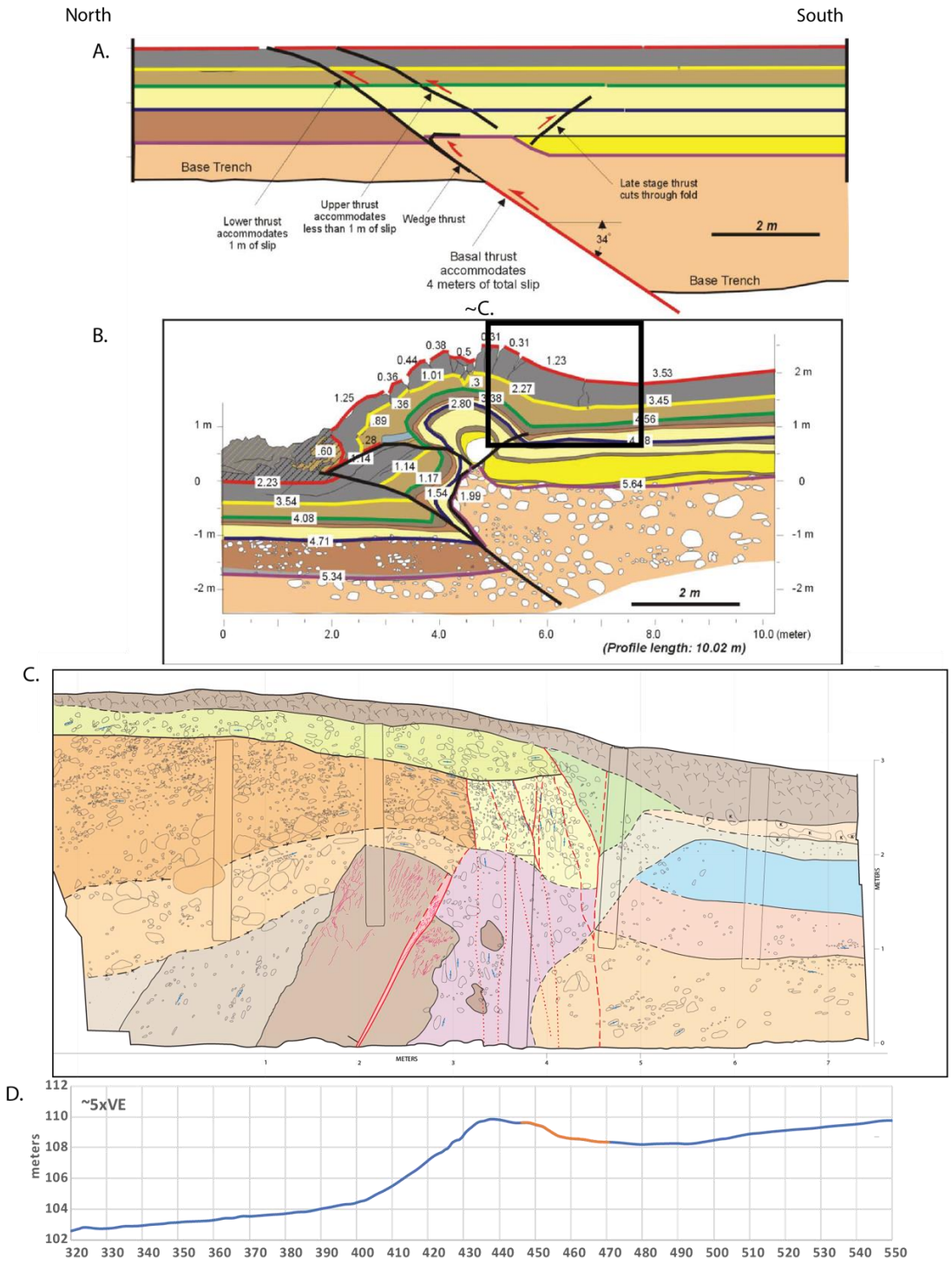

Appendix G: Northeast-southwest interpretive geologic cross section in northern California. Open circles show epicenters and select focal mechanisms of earthquakes from Magee (1994). Proposed reinterpretation of the Goose Lake fault drawn in red, dipping south, and rooting in the Russ fault. Location of cross section shown in Appendix H. Modified from McLaughlin and others (2000).

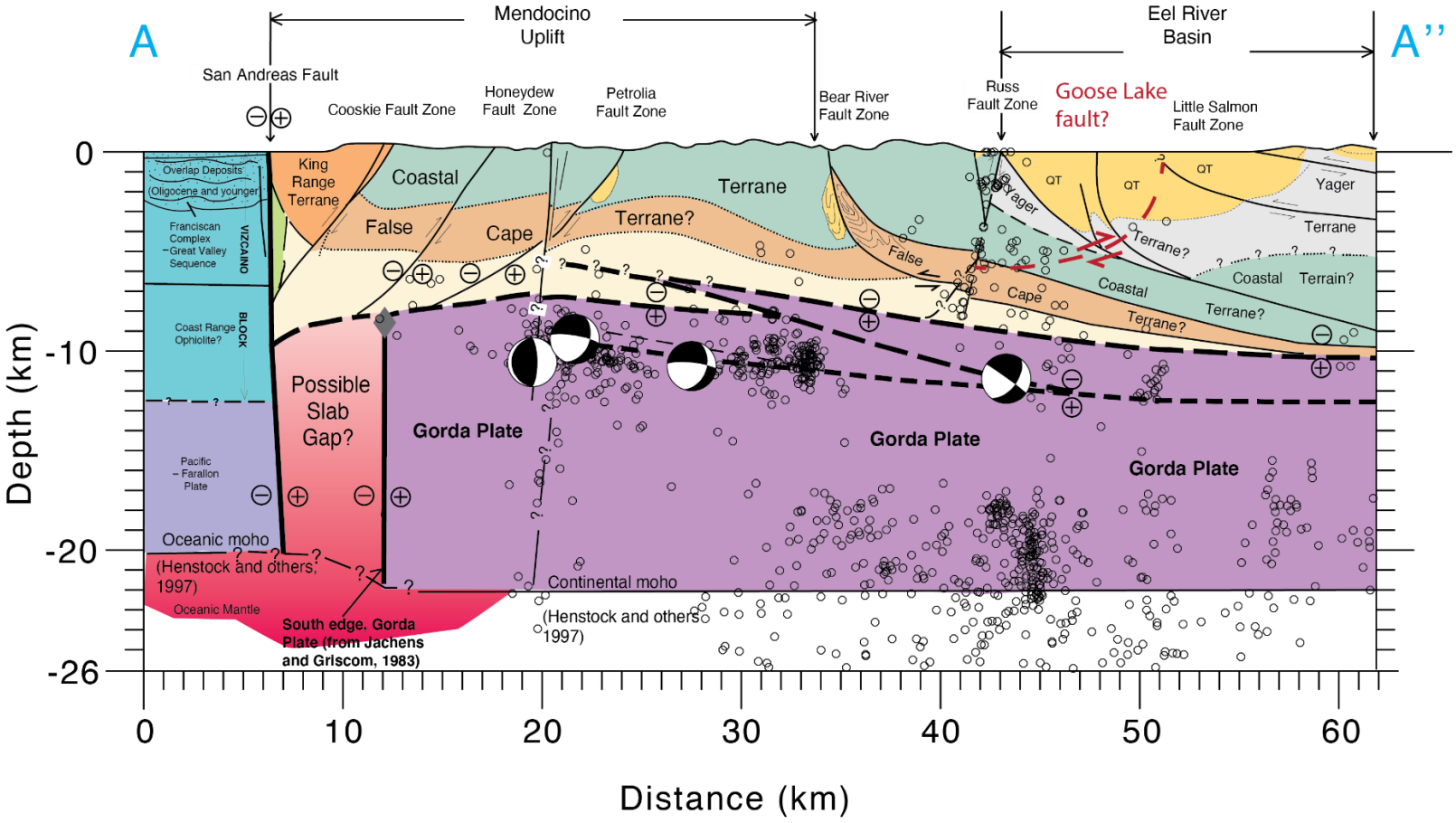

Appendix H: Map of seismicity in northern California. Blue box locates geologic cross section depicted in Appendix G with the Goose Lake fault called out. Modified from McLaughlin and others (2000).